

# Distant galaxy clusters in a deep XMM-Newton field within the CFHTLS D4\*†‡§

A. de Hoon<sup>1</sup>, G. Lamer<sup>1</sup>, A. Schwobe<sup>1</sup>, M. Mühlegger<sup>2</sup>, R. Fassbender<sup>2</sup>, H. Böhringer<sup>2</sup>, M. Lerchster<sup>2</sup>, A. Nastasi<sup>2</sup>, R. Šuhada<sup>6</sup>, M. Verdugo<sup>2,7</sup>, J.P. Dietrich<sup>6</sup>, F. Brimiouille<sup>6</sup>, P. Rosati<sup>2</sup>, D. Pierini<sup>¶</sup>, J.S. Santos<sup>3</sup>, H. Quintana<sup>4</sup>, A. Rabitz<sup>1</sup>, and A. Takey<sup>1,5</sup>

<sup>1</sup> Leibniz-Institut für Astrophysik Potsdam (AIP), An der Sternwarte 16, D-14482 Potsdam, Germany  
e-mail: arjen@aip.de

<sup>2</sup> Max-Planck-Institut für extraterrestrische Physik, Giessenbachstraße, 85748 Garching, Germany

<sup>3</sup> European Space Astronomy Center (ESAC)/ESA, Madrid, Spain

<sup>4</sup> Departamento de Astronomía y Astrofísica, Pontificia Universidad Católica de Chile, Casilla 306, Santiago 22, Chile

<sup>5</sup> National Research Institute of Astronomy and Geophysics (NRIAG), Helwan, Cairo, Egypt

<sup>6</sup> University Observatory Munich, Ludwig-Maximilians University Munich, Scheinerstr. 1, 81679 Munich, Germany

<sup>7</sup> Institut für Astronomie, Universität Wien, Universitätsring 1, 1010, Wien

received 17 Sept. 2012; accepted 07 Dec. 2012

## ABSTRACT

**Aims.** The XMM-Newton Distant Cluster Project (XDCP) aims at the identification of a well defined sample of X-ray selected clusters of galaxies at redshifts  $z \geq 0.8$ . As part of this project, we analyse the deep XMM-Newton exposure covering one of the CFHTLS deep fields to quantify the cluster content. We validate the optical follow-up strategy as well as the X-ray selection function.

**Methods.** We searched for extended X-ray sources in archival XMM-Newton EPIC observations. Multi-band optical imaging was performed to select high redshift cluster candidates among the extended X-ray sources. Here we present a catalogue of the extended sources in one the deepest  $\sim 250$  ksec XMM-Newton fields targeting LBQS 2212-1759 covering  $\sim 0.2^\circ$ . The cluster identification is based on deep imaging with the ESO VLT and from the CFHT legacy survey, among others. The confirmation of cluster candidates is done by VLT/FORS2 multi-object spectroscopy. Photometric redshifts from the CFHTLS D4 were utilised to confirm the effectiveness of the X-ray cluster selection method. The survey sensitivity was computed with extensive Monte-Carlo simulations.

**Results.** At a flux limit of  $S_{0.5-2.0 \text{ keV}} \sim 2.5 \cdot 10^{-15} \text{ erg s}^{-1}$  we achieve a completeness level higher than 50% in an area of  $\sim 0.13^\circ$ . We detect six galaxy clusters above this limit with optical counterparts, of which 5 are new spectroscopic discoveries. Two newly discovered X-ray luminous galaxy clusters are at  $z \geq 1.0$ , another two at  $z = 0.41$ , and one at  $z = 0.34$ . For the most distant X-ray selected cluster in this field at  $z = 1.45$ , we find additional (active) member galaxies from both X-ray and spectroscopic data. Additionally, we find evidence of large-scale structures at moderate redshifts of  $z = 0.41$  and  $z = 0.34$ .

**Conclusions.** The quest for distant clusters in archival XMM-Newton data has led to detection of six clusters in a single field, making XMM-Newton an outstanding tool for cluster surveys. Three of these clusters are at  $z \geq 1$ , which emphasises the valuable contribution of small, yet deep surveys to cosmology. Beta models are appropriate descriptions of the cluster surface brightness when performing cluster detection simulations to compute the X-ray selection function. The constructed  $\log N - \log S$  tends to favour a scenario where no evolution in the cluster X-ray luminosity function (XLF) takes place.

**Key words.** cosmology: observations – cosmology: large scale structure of universe – cosmology: dark matter – surveys – X-rays: galaxies: clusters

Send offprint requests to: A. de Hoon

\* This work made use of observations made with ESO Very Large Telescope at the La Silla Observatory under the programmes 072.A-0706(A), 073.A-0737(A), 079.A-0369(C), and 080.A-0659(A)

† XMM-Newton, an ESA science mission with instruments and contributions directly funded by ESA Member States and NASA

‡ Tables 2 and 5 are only available in electronic form at the CDS via anonymous ftp to cdsarc.u-strasbg.fr (130.79.128.5) or via <http://cdsweb.u-strasbg.fr/cgi-bin/qcat?J/A+A/>

§ Full-resolution images are available only in the published version of the manuscript in A&A.

¶ Freelance astronomer

## 1. Introduction

Clusters of galaxies are the largest gravitationally bound objects in the Universe and are tracers of the cosmic structure. Since their formation and evolution depends sensitively on the cosmological parameters, they are strong cosmological probes. Identification of clusters from X-ray surveys is currently the best method of constructing well defined samples of galaxy clusters for cosmological studies. The X-ray emission of the intracluster gas depends mostly on the square of the gas density. Owing to the peaked gas density distribution of clusters, the X-ray emission is more compact than the distribution of cluster galaxies, hence less

affected by projection effects. For these reasons the X-ray luminosity is a good proxy of the total cluster mass.

The identification of ROSAT X-ray sources has resulted in large samples of local clusters (e.g. Böhringer et al. 2004, REFLEX) and a limited number of clusters at intermediate redshifts  $z > 0.4$  (e.g. Vikhlinin et al. 1998). Only five distant clusters beyond  $z = 1$  have been found among the ROSAT sources, most of them in the ROSAT Deep Cluster Survey (Rosati et al. 1998, RDCS).

Among the large number of extended sources serendipitously detected by XMM-Newton (Schwope et al. 2004; Lloyd-Davies et al. 2011; Takey et al. 2011) one can expect a significant fraction of distant clusters of galaxies. To date, about 40 clusters beyond redshift  $z \gtrsim 1$  and about 10  $z \gtrsim 1.4$  are known, of which IDCS J1426.5+3508 at  $z = 1.75$  (Stanford et al. 2012), ClG J0218.3-0510 at  $z = 1.62$  (Papovich et al. 2010; Tanaka et al. 2010; Pierre et al. 2011), XMMU J0338.8+0021 at  $z = 1.49$  (Nastasi et al. 2011), LH146 at  $z = 1.75$  (Henry et al. 2010), XMMU J0044.0-2033 at  $z = 1.58$  (Santos et al. 2011), and XMMU J1007.4+1237 at  $z = 1.56$  (Fassbender et al. 2011b) are the most distant ones. There have also been claims of even more distant clusters at  $z \sim 2$  (Andreon et al. 2009; Gobat et al. 2011); however, these sources lack either a clear X-ray detection or spectroscopic confirmation.

We are conducting a focussed project on the identification of distant ( $z \geq 0.8$ ) clusters from serendipitously detected XMM-Newton sources, the XMM-Newton Distant Cluster Project (XDCP, Böhringer et al. 2005; Lamer et al. 2006; Fassbender et al. 2011a). An early success was our discovery of the most distant cluster of that time, XMMU 2235.3-2557 at  $z = 1.39$  (Mullis et al. 2005). To date the XDCP has been contributing half of the known sample of distant galaxy clusters. The sample contains 22 X-ray bright sources in the redshift range  $0.9 < z < 1.6$  alone (Fassbender et al. 2011a).

In the current paper we report on the extended X-ray sources found in the field of the broad absorption line (BAL) QSO LBQS 2212-1759. This object has been repeatedly targetted with XMM-Newton, so that the field features one of the deepest XMM-Newton EPIC (European Photon Imaging Camera) exposures taken at that point. This field also received deep optical imaging coverage by the ESO Imaging Survey (EIS field XMM-07, Dietrich et al. (2006), Mignano et al. (2007)) and the Canada-France-Hawaii Telescope (CFHT) legacy survey (LS) deep field four (D4). Furthermore, we have performed extensive spectroscopic follow-up with VLT/FORS2 to confirm cluster membership. We supply a complete X-ray source list of the stacked X-ray images for point sources as *Online material* in Table 2. However, in this paper, we focus on the content of only extended sources (Table 3).

The paper is structured as follows. In Section 2 we describe the X-ray source detection and the X-ray spectral analysis of the brightest extended sources. Section 3 gives an overview of the optical data available for the field and describes the galaxies over-densities in photometric redshift space derived from them. The spectroscopic confirmation of the cluster candidates is presented next in Section 4. Section 5 presents the optical identifications of the extended X-ray sources and the cluster redshifts. In the same section, the identification of the individual objects is discussed. The cosmological interpretation of our results is finally presented in Section 6.

Table 1: Summary of XMM-Newton observations.

ObsID	Date	good exposure time[s]		
		MOS1	MOS2	PN
0106660101	2000-11-17	57229	57273	54829
0106660201	2000-11-18	52177	52073	38247
0106660401	2001-11-16	33350	33561	-
0106660501	2001-11-17	8063	8091	5665
0106660601	2001-11-17	100790	101211	84178
total		251609	252209	182919

We adopt a cosmology of  $H_0 = 70 \text{ km s}^{-1} \text{ Mpc}^{-1}$ ,  $\Omega_M = 0.3$ , and  $\Omega_\Lambda = 0.7$  and magnitudes are in the AB system.

## 2. XMM-Newton observations

### 2.1. X-ray data reduction and source detection

XMM-Newton has repeatedly targetted (yet never detected) the BAL QSO LBQS 2212-1759 (Clavel et al. 2006). The field received a total good exposure of 250 ksec and is thus one of the deepest XMM fields. We retrieved the EPIC data sets from the public XMM archive (XSA) and processed the data from observation data files (ODFs) with the XMM Science Analysis Software (XMM-SAS v. 6.5)<sup>1</sup>. Source detection runs with one of the latest versions XMM-SAS v. 11 show no major changes with respect to the source list used in this work. We therefore remain with the older version for consistency and comparison with the 2XMM catalogue.

To screen the data for periods of high particle background, we created light curves of the high energy (7-15 keV) events for each of the three EPIC cameras. Periods where the count rate was more than 30% higher than the median rate were excluded from the later analysis. Table 1 shows the remaining exposure times of cleaned data for the individual pointing.

The event lists of each observation were transformed to a common astrometric frame (using the XMM-SAS task `attcalc`) and images in the five standard XMM-Newton energy bands (Watson et al. (2009), *band 1*: 0.2–0.5 keV, *band 2*: 0.5–1.0 keV, *band 3*: 1.0–2.0 keV, *band 4*: 2.0–4.5 keV, *band 5*: 4.5–12.0 keV) were binned for each camera and exposure. These bands differ from the energy bands (with a focus on 0.35–2.4 keV) usually used within the XDCP collaboration (Fassbender et al. 2011a).

For each of these images, an exposure map, background map, and detection mask were created using the respective XMM-SAS source detection tasks. Subsequently, the science images, exposure maps, and background maps of the individual exposures were added, creating one image for each of the three cameras and five energy bands.

In the softest band (0.2–0.5 keV) some of the EPIC detectors show spatially and temporally variable background features that can lead to spurious detections of extended sources. On the other hand, the thermal spectra of galaxy clusters only have a small fraction of their count rates in the hardest band beyond 4.5 keV. Therefore we restricted the detection of extended sources to the energy bands 2-4.

Source detection with the XMM-SAS tasks `ebxdetect` and `emldetect` was performed simultaneously on the nine

<sup>1</sup> XMM-SAS version 6.5 was the prototypical release used to construct the 2XMM catalogue (Watson et al. 2009)

images from three cameras and three energy bands. The task `eboxdetect` applies a sliding box detection algorithm to the input images. The resulting list is passed to the task `emldetect`, which fits the calibration PSF, optionally convolved with an extent model, to each input source. Extended sources were modelled using a King profile of the form

$$f(x, y) = \left(1 + \frac{(x - x_0)^2 + (y - y_0)^2}{r_c^2}\right)^{-3/2} \quad (1)$$

with core radii between  $r_c = [4.0'' - 80.0'']$  as the model's extent parameter space.  $x - x_0$  and  $y - y_0$  are pixel coordinates relative to the central pixel of the object considered. The thresholds for the detection likelihoods were set to  $L = 5.0$  for `eboxdetect` and  $L = 6.0$  for `emldetect`, with  $L = -\ln(P_{\text{false}})$ . This corresponds to probabilities of false detection of  $P = 6.7 \cdot 10^{-3}$  and  $P = 2.5 \cdot 10^{-3}$ .

The `emldetect` output source list contains 264 sources<sup>2</sup>, of which nine are indicated to be extended. These objects are numbered in Figure 1. Table 3 lists the extended sources with their basic X-ray parameters derived from `emldetect` and sorted according to source counts. Spectral X-ray properties normalised to physical scales are found in Table 4.

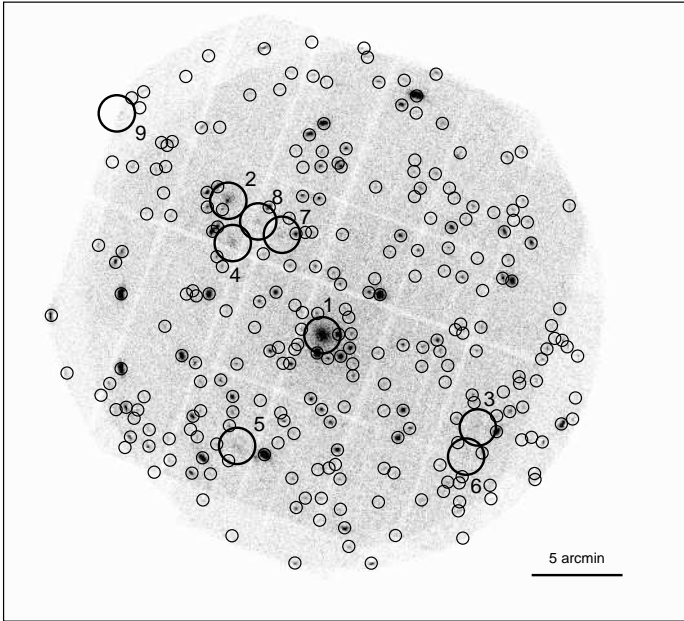


Fig. 1: The stacked EPIC image in the 0.2-2.0 keV band with detected point sources (small circles) and extended sources (large circles) labelled from 1 to 9.

## 2.2. X-ray spectra and redshift estimates

Thanks to the deep exposure in the field, several of the extended sources were detected with more than 1 000 source counts (see Table 3). We therefore attempted to estimate the redshifts of the brightest cluster candidates by fitting

<sup>2</sup> The complete source list of point source is found as *Online material* in Table 2. The extended source, however, are listed in Table 3.

EPIC spectra with plasma spectra templates, keeping redshifts and temperatures as free parameters. With the same method we derived metallicities for those clusters where it was feasible.

We extracted spectra (using `XMM-SAS v.10.0`) for all the sources with  $> 400$  counts (i.e. sources ext#1-#6). Due to the low count rates ( $0.01 - 0.05$  cts  $\text{sec}^{-1}$ ) and the extended nature of the sources the background fraction in the extracted spectra is relatively high. Therefore the regions for source and background extraction were manually selected to avoid systematic errors introduced by chip gaps, etc., and to avoid contamination by unrelated X-ray sources. The data were rendered and fitted through `XSPEC` using C statistics. We applied single `MEKAL` models corrected for galactic absorption (`tbabs`).

The spectral fits enable us to get a handle on the clusters redshift, which initially drove our follow-up programme. Some X-ray spectra enabled tight constraints on the distance, as in the case of source ext#1, which is the only source alone the iron line has been detected. Others merely confirmed the “high” redshift  $z \gtrsim 1$  nature of the cluster as displayed in Figures ??-??. An overview of spectral X-ray properties is presented in Table 4. The individual results are discussed both in Section 5 for each confirmed cluster individually and in the appendix (Sect. ??). The spectral properties in the context of the proper flux determination are discussed in the next section.

## 2.3. Flux determination

To enable comparisons of our results with previous findings from other works requires a flux measurement within a fixed radius. There,  $S_\Delta$  is the flux within  $R_\Delta$ , where  $\Delta$  is defined as the average density of the intracluster medium (ICM) relative to the critical density of the Universe at a given redshift. The flux  $S_{500}$  is commonly indicated, however, in most cases not directly measurable, owing to the sensitivity of the instruments, the background level, point source contamination and chip gaps. The fluxes from Table 3 are the results of the source detection, and they correspond to fitted beta models integrated over a theoretically infinite radius.

To obtain  $S_{500}$ , we apply an iterative approach. This method is described in detail in Šuhada et al. (2012) and Takey et al. (2011). To estimate  $M_{500}$  we apply the empirical scaling relation from Vikhlinin et al. (2009). Since these authors measure the flux in the energy band 0.5 – 2 keV as well, no conversion is required. Appropriately, the evolution of the  $L_X - M$  relation deduced in Vikhlinin et al. (2009) is compatible with the findings from Reichert et al. (2011), which both allow for a non-evolution scenario; i.e., the luminosity of clusters does not change self-similarly with redshift. In the self-similar case, the evolution factor is  $E(z)^{-7/4}$ . The physical parameters used in the iterative approach are computed using the following equations:

$$M_{500} = 1.64 \times 10^{-13} L_{500}^{0.62} E(z)^{-1.15} \left(\frac{h}{0.72}\right)^{0.24} \quad (2)$$

$$R_{500} = \left(\frac{3 M_{500}}{4\pi 500 \rho(z)}\right)^{\frac{1}{3}} \quad (3)$$

$$r_c = 0.07 R_{500} T_{500}^{0.63}, \quad (4)$$

Table 3: Extended X-ray sources properties from source detection. CTS stands for photon counts, CR for count rate, S for flux, EXT\_LIKE is the extent likelihood, and DET\_LIKE the detection likelihood. The core radius is denoted by  $r_c$ .

Seq. #	Source XMMU J..	CTS	CR <sub>0.5–4.5 keV</sub> 10 <sup>−3</sup> s <sup>−1</sup>	S <sub>0.5–2.0 keV</sub> 10 <sup>−15</sup> erg cm <sup>−2</sup> s <sup>−1</sup>	$r_c$ arcsec	EXT_LIKE	DET_LIKE
1	221536.8-174534	7982	42.3 ± 1.00	36.3 ± 0.9	17.8 ± 0.5	696.6	2278.7
2	221558.6-173810	1807	17.3 ± 0.70	13.3 ± 0.6	10.8 ± 0.6	154.0	580.4
3	221500.9-175038	1055	9.19 ± 0.91	8.65 ± 0.73	25.9 ± 2.1	42.2	80.5
4	221557.5-174029	909	8.79 ± 0.65	7.26 ± 0.53	14.9 ± 1.1	61.7	136.8
5	221556.6-175139	689	6.55 ± 0.71	5.69 ± 0.58	16.8 ± 1.8	26.3	61.6
6	221503.6-175215	485	4.75 ± 0.74	3.76 ± 0.62	19.4 ± 3.0	7.3	21.3
7	221546.2-174002	384	2.66 ± 0.36	1.88 ± 0.29	10.5 ± 1.7	6.6	24.8
8	221551.7-173918	384	3.32 ± 0.41	1.98 ± 0.32	9.3 ± 1.5	8.1	35.0
9	221624.3-173321	380	24.6 ± 3.60	29.9 ± 4.3	20.1 ± 3.9	19.7	64.4

where  $\rho(z)$  is the critical density of the Universe, and  $h$  the normalised Hubble parameter. The evolution factor and  $\rho(z)$  are defined as

$$E(z) = \sqrt{\Omega_m(1+z)^3 + \Omega_a} \quad (5)$$

$$\rho(z) = \frac{3E(z)^2 H(z)^2}{8\pi G} \quad (6)$$

Given the luminosity from the spectral fit, we can make an estimation for  $M_{500}$  by applying equation (2) and setting  $h$  to 0.70. The errors on the mass are the simple propagation of the luminosity uncertainties. From this quantity we derive  $R_{500}$  using equation (3). Since the cluster-specific core radius, which largely determines the shape of the beta model, is only mildly realistically described by the `emldetect` output, we use the empirical relation, equation (4), from the cosmic evolution survey (COSMOS, Finoguenov et al. 2007) to re-estimate  $r_c$ . The essential step in this procedure is to determine what fraction of  $R_{500}$  we have covered in the area from which the spectrum has been extracted.

To do so, we synthesise beta models as in equation (7). The beta model is essentially a King profile from equation (1), and it describes the surface brightness profile of a cluster, determined uniquely by the core radius  $r_c$ , provided  $\beta$  is known. By varying the radius  $R$ , which is computed using equation (3), we determine the fraction of the surface brightness enclosed, which equals the luminosity correction for a certain radius.

When this quantity converges, i.e.  $R = R_{500}$ , after several iterations (typically 2) we assume we have obtained the true  $R_{500}$ , and hence  $L_{500}$  proper. On average the spectral extraction radius has been 2.2 times smaller than  $R_{500}$ . The resulting values are presented in Table 4 using spectral fluxes.

$$S(R) = S_0 \left( 1 + \left( \frac{R}{r_c} \right)^2 \right)^{-3\beta + \frac{1}{2}}. \quad (7)$$

We fix the temperature at the value from the spectral fit. We emphasise, that all source detection chains in this work assume  $\beta = \frac{2}{3} \approx 0.67$ . The factor between  $L_{0.5-2.0 \text{ keV}}$  and  $L_{500}$  in Table 4 is applied to convert  $S_{0.5-2.0 \text{ keV}}$  into  $S_{500}$ .

### 3. Optical imaging

The field of LBQS 2212-1759 has been the target of various imaging programmes. This section describes campaigns

that have been launched as part of this study and the archival data analysed in supplement. An overview of the sky coverage is presented in Figure 2. In this paper, only the area enclosed by the central XMM-Newton pointing (blue circle, solid line) is considered.

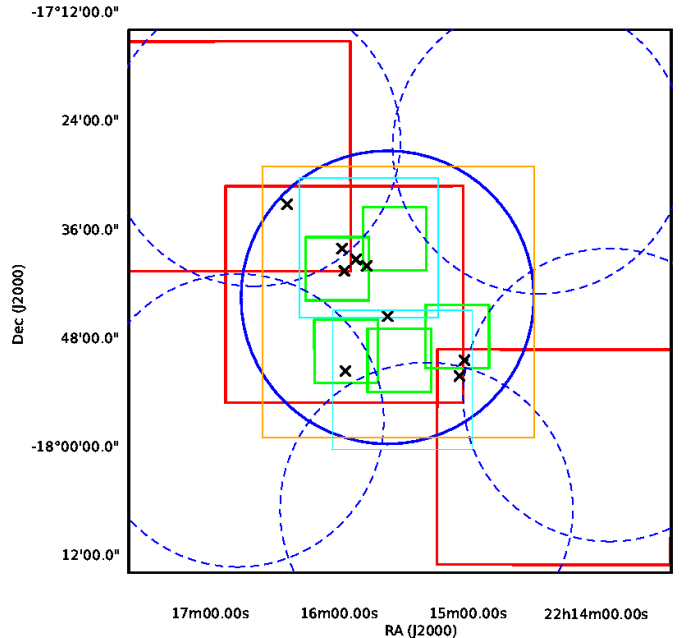


Fig. 2: Sky coverage of imaging campaigns. *Black*: The optical 1° CFHTLS D4 field. *Orange*: The *BVR* sky projection as imaged by the WFI. *Red*: The NIR WIRcam supplementary coverage. *Cyan*: The NIR observations made at Calar Alto. *Blue*: XMM-Newton pointings. The dashed circles represent the 2007 study (P.I. K. Nandra) covering the entire D4 in X-rays with  $\sim 30 - 40$  ks exposures (Bielby et al. 2010). *Green*: VLT-FORS2 pointings used for initial detection. The crosses indicate the position of all clusters found.

First, the field was selected for deep imaging observations in the *B*, *V*, *R*, and *I* bands with the Wide Field Imager (WFI) at the 2.2m ESO/MPIA telescope as part of the ESO Imaging Survey (Dietrich et al. 2006). The exposure time in the *R*-band was augmented by a guest observer programme for the Bonn weak lensing survey (Dietrich et al. 2007, BLOX). In Oct. and Nov. 2006, a NIR campaign was run in the bands *z* and *H* with the Omega

Table 4: Extended X-ray sources. X-ray properties from spectral fitting and the iterative method (Sect. 2.3). Sources ext#7-#9 have been excluded, for they are not galaxy clusters. In case of non-symmetric errors, the largest deviation is presented. The first four columns display spectral measurements.  $r_{\text{spec}}$  is the radius in which the spectrum has been extracted.  $R_{500}$ ,  $L_{500}$  and  $M_{500}$  are products of the iterative method.

#	$S_{0.5-2.0 \text{ keV}}$ $10^{-15} \text{ erg cm}^{-2} \text{ s}^{-1}$	$L_{0.5-2.0 \text{ keV}}$ $10^{42} \text{ erg s}^{-1}$	$T$ keV	Abund. $Z_{\odot}$	$r_{\text{spec}}$ arcsec	$R_{500}$ Mpc	$L_{500}$ $10^{42} \text{ erg s}^{-1}$	$M_{500}$ $10^{14} M_{\odot}$
1	$21.32 \pm 0.03$	$11.7 \pm 0.02$	$2.14 \pm 0.07$	$0.34^{+0.06}_{-0.09}$	48	0.56	$14.5 \pm 0.3$	0.79
2	$6.28 \pm 0.03$	$54.0 \pm 1.50$	$4.40 \pm 0.48$		23	0.39	$70.7 \pm 5.3$	1.07
3	$2.28 \pm 0.01$	$0.86 \pm 0.002$	$1.42 \pm 0.18$		29	0.40	$1.69 \pm 0.09$	0.17
4	$2.87 \pm 0.28$	$13.4 \pm 0.13$	$2.06 \pm 0.20$		23	0.41	$21.6 \pm 4.0$	0.57
5	$2.93 \pm 0.32$	$25.1 \pm 0.27$	$2.00 \pm 0.21$		26	0.39	$33.5 \pm 7.9$	0.71
6	$1.05 \pm 0.01$	$0.59 \pm 0.07$	$1.84 \pm 0.86^a$		30	0.34	$0.92 \pm 0.2$	0.12

**Notes.** <sup>(a)</sup> Tentative value, due to low signal-to-noise.

2000 camera at the Calar Alto 3.5m telescope. Both ESO data sets have been used for the initial clusters identification. For all final photometric analysis in this section, however, we rely solely on the data from the CFHTLS, due to its supremacy. We describe the data reduction in Section 3.1. Section 3.2 describes the retrieval of photometric redshifts, which we apply to find over-densities of galaxies in Section 3.3.

### 3.1. CFHT data

We make use of *ugriz* archival data taken with the MegaPrime/MegaCam instrument mounted at the prime focus at the 3.6m Canada-France-Hawaii Telescope (CFHT). This instrument has a field of view of  $1 \times 1 \text{ deg}^2$  and a scale of 0.187 arcsec per pixel.

We made use of data located in the deep field D4 of the CFHT Legacy Survey (CFHTLS), which is part of the CFHT Supernova Legacy Survey (SNLS) and observations are still ongoing. We retrieved the data from the Elixir system<sup>3</sup> in a preprocessed form and further processed it as described in Erben et al. (2009)<sup>4</sup>. This reduction is independent of the official releases by the CFHTLS collaboration (Ilbert et al. 2006; Coupon et al. 2009).

The photometry was performed with *sextractor* (Bertin & Arnouts 1996) in dual mode using the *i*-band image as a detection frame. We measured magnitudes in apertures of 1.86 arcsec of diameter in seeing-matched images. The derived magnitudes were used to derive colours, SED classification, and photometric redshifts (see below). We also made use of deep near-infrared data (*JH* & *Ks* bands) with the WIRcam (also at CFHT). The data is part of the WIRcam Deep Survey (see Bielby et al. 2010) and covers a significant portion of most of the deep XMM-Newton field. This data is important for obtaining precise photometric redshifts at high redshift as important continuum features (e.g. the 4000 Å break) are shifted to the near-infrared.

### 3.2. Photometric redshifts

In this paper we use the multi-band imaging (*u\*g\*r'i'z'JHKs*) and photometric galaxy redshifts from

the CFHTLS to identify cluster counterparts of the extended X-ray sources and to measure their photometric redshifts. We used the code *PHOTO-z* (Bender et al. 2001) to estimate the photometric redshifts, with a set of 31 SED templates (see Brimiouille et al. 2008; Lerchster et al. 2011, for details).

We used the results from the spectroscopic programme (Section 4) to calibrate our photometric redshift estimates by applying zero-point offsets (typical values are  $\sim 0.01..0.1$  mag). A total of 106 spectra fulfil the quality criteria (i.e. objects with reliable photometric *and* spectroscopic redshifts). The fraction of catastrophic outliers is defined as  $\eta = |z_{\text{spec}} - z_{\text{phot}}|/(1 + z_{\text{spec}}) > 0.15$ , which is 2.8% in our case. The redshift accuracy is measured with the normalised median absolute deviation,  $\sigma = 1.48 \times \text{median}(|\Delta z|/(1 + z)) = 0.037$ , where  $\Delta z = z_{\text{spec}} - z_{\text{phot}}$  and  $z$  is spectroscopic. The value of  $\sigma$  is identical to the standard deviation of  $|\Delta z|/(1 + z)$ .

### 3.3. Galaxy over-densities

From the photometric redshift information we measured the projected galaxy over-density in overlapping redshift intervals of  $\Delta z = 0.05$ . The purpose of this procedure was to qualitatively illustrate the completeness of the X-ray selection technique as a method to identify clusters of galaxies. Therefore we set a relatively high detection threshold in order to pick up only the most significant density peaks.

We computed the mean galaxy density in boxes of 400 kpc a side, which is enlarged to 500 kpc for redshifts  $z > 0.9$ , masking out regions affected by bright stars. At redshifts beyond  $z > 0.9$  clusters are thought to be increasingly less relaxed. Therefore, the need arises to search for the associated galaxies in a larger physical volume. The values of  $\Delta z$ , the box size and the critical redshift where the box size changes have been tuned to maximise the detection of the already known clusters in this field from this work. We consider only galaxies with a photometric redshift error  $\delta z < 0.1$ . We compared the number of galaxies in the box to the assumed Poisson distributed background, which is taken to be the mean galaxy count in the field considered. The likelihood (equation (8)) was computed taking the negative natural logarithm of the incomplete gamma function  $P(a, x)$  as defined in equation (9). The incomplete gamma function is an integral, which is applied to computing the likelihood that a given distribution  $x$  (i.e. the number of

<sup>3</sup> <http://www.cfht.hawaii.edu/Instruments/Elixir/home.html>

<sup>4</sup> The full procedure of data reduction and calibration will be described in Brimiouille et al. (2013, in prep.), see also Brimiouille et al. (2008).

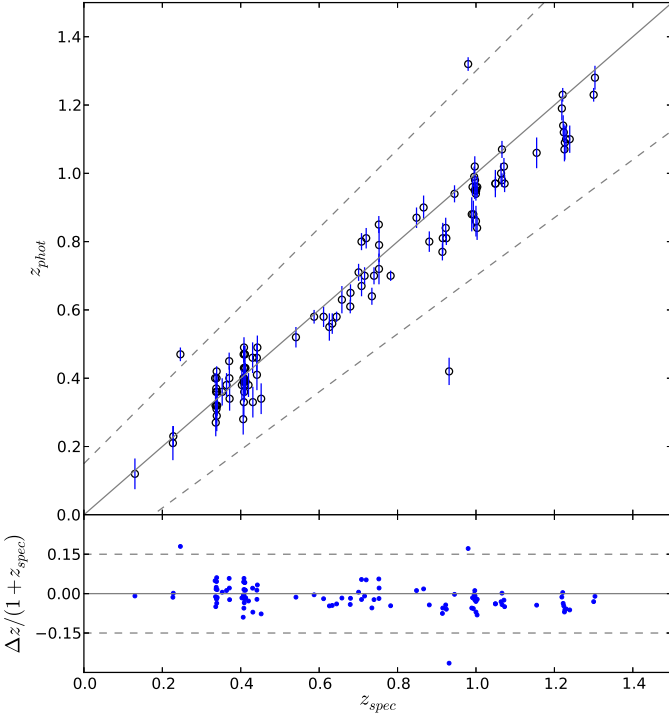


Fig. 3: Photometric redshifts, plotted against the spectroscopic ones. The vertical dashes are the photometric redshift errors. The dashed lines are for  $z_{phot} = z_{spec} \pm 0.15$  ( $1 + z_{spec}$ ).

galaxies is the box) is exceeding Poissonian noise  $a$  (Cash 1979).

$$L = -\ln P(a, x) \quad (8)$$

with

$$P(a, x) = \frac{1}{\Gamma(a)} \int_0^x e^{-t} t^{a-1} dt, \quad (9)$$

where  $\Gamma(a)$  is the gamma function. This method of “source finding” is similar to the XMM-SAS task `eboxdetect` (Watson et al. 2009) also described in Section 2.1. The resulting map is displayed in Figure 4 as contours on the stacked X-ray image. The redshift intervals are chosen to overlap in order to prevent a search bias that would occur when clusters fall exactly between two intervals. Since the redshift error cut is set to 0.1, some galaxy over-densities are expected to show up in multiple adjacent redshift bins. We have assumed a nominal redshift error of 0.001 for all galaxies, ensuring that each galaxy appears in one redshift bin only. All confirmed X-ray selected clusters from Table 7 are retrieved at the appropriate redshifts. That is, all spectroscopically confirmed clusters are found in a redshift interval around the nominal redshift taking the spread in the photo- $z$  accuracy into account (see Figure 3), of which typical values amount to about 5%.

We define the photometric redshift  $z_{phot}$  of the clusters as the *mean* of all galaxies meeting the above-mentioned selection criteria (i.e. photometric accuracy and spatial distribution), having  $\frac{\Delta z_1}{1+z_{mid}} < 0.05$ , where  $\Delta z_1 = |z^* - z_{mid}|$ .  $z_{mid}$  is the middle of the redshift bin containing the largest number of galaxies, whereas  $z^*$  is the photometric redshift of each individual galaxy. The relative dif-

ference (in %) in Table 7 is defined as  $\frac{\Delta z_2}{1+z_{spec}}$ , where  $\Delta z_2 = z_{phot} - z_{spec}$ . For the nearby clusters in our sample,  $z_{phot}$  tends to be slightly overestimated, while the high redshift ones the photometric redshift is somewhat lower than the spectroscopic one. The redshift bin, in which the galaxy signal is strongest (i.e. highest likelihood) is selected for display in Figure 4. This quantity is identical neither to  $z_{mid}$  nor to  $z_{phot}$  due to different treatments of background galaxies. Nonetheless, they remain similar.

The clusters are indicated with colour-coded contours reflecting the redshift and the over-density likelihood. We display only significant<sup>5</sup> over-densities having  $L > 10$ , within the field of view of the XMM-Newton pointing. A selection of clusters found in previous publications (Bielby et al. 2010; Olsen et al. 2007; Adami et al. 2010) are also referred to in Figure 4. The most distant (Stanford et al. 2006) cluster is detected by all groups except for Adami et al. (2010), whereas some other structures, i.e. system ext#6 and the new, possibly spurious structure (red arrow in Figure 4), are found solely in this work. Source ext#4 is also found by Adami et al. (2010) at  $z_{phot} = 0.95$ . Finally, we retrieve all X-ray selected clusters as optical over-densities. Additionally, we find a significant over-density, that is indicated by the arrow in Figure 4, which could not be associated with an X-ray source at an off-axis angle  $\sim 14$  arcmin. The optical data suggest a detection due to an projection effect, since no conglomeration of *red* galaxies is evident.

Olsen et al. (2007) have applied the Postman matched filter (MF, Postman et al. 1996) to search for optically selected clusters of galaxies in the CFHTLS deep fields. In the overlap of field D4 with the XMM-Newton FoV they found eight clusters with redshifts ranging from  $z = 0.3$  to  $z = 1.1$ . These structures are partially retrieved by us as seen in Figure 4. Grove et al. (2009) have extended the sample by including the  $z'$ -band. This has led to an enhanced detection of distant clusters, which, however, are not discussed further in this work.

In a similar fashion Adami et al. (2010) detect ten clusters within the common area from galaxy density maps resulting from an adaptive kernel algorithm working on slices in (photometric) redshift space. The papers from Olsen et al. (2007), Grove et al. (2009), and Adami et al. (2010) are comparable to one another in various ways, and for the same reasons different from our study. First of all, all base their density map on a single band detection (for instance the  $i'$  band), secondly, use a similar detection algorithm for optical over-densities, and thirdly, none perform an X-ray source detection, which automatically points them to a larger quantity of less massive optical clusters. Last, the works addressed above are restricted to the optical  $u^*g'r'i'z'$  data and therefore are expected to remain less sensitive to the more distant clusters in the field.

Gavazzi & Soucail (2007) use the  $i'$ -band images for weak lensing mass reconstruction. In the D4 field they find one significant mass peak, which is outside the XMM-Newton FoV.

A more direct comparison to our work is given by Bielby et al. (2010), who applied a red sequence finder to their wavelet-detected extended X-ray sources in D4. This team focussed on groups and clusters at high red-

<sup>5</sup>  $L = 10$  corresponds to a significance  $> 99.9\%$  or roughly  $5\sigma$  in Gaussian statistics.



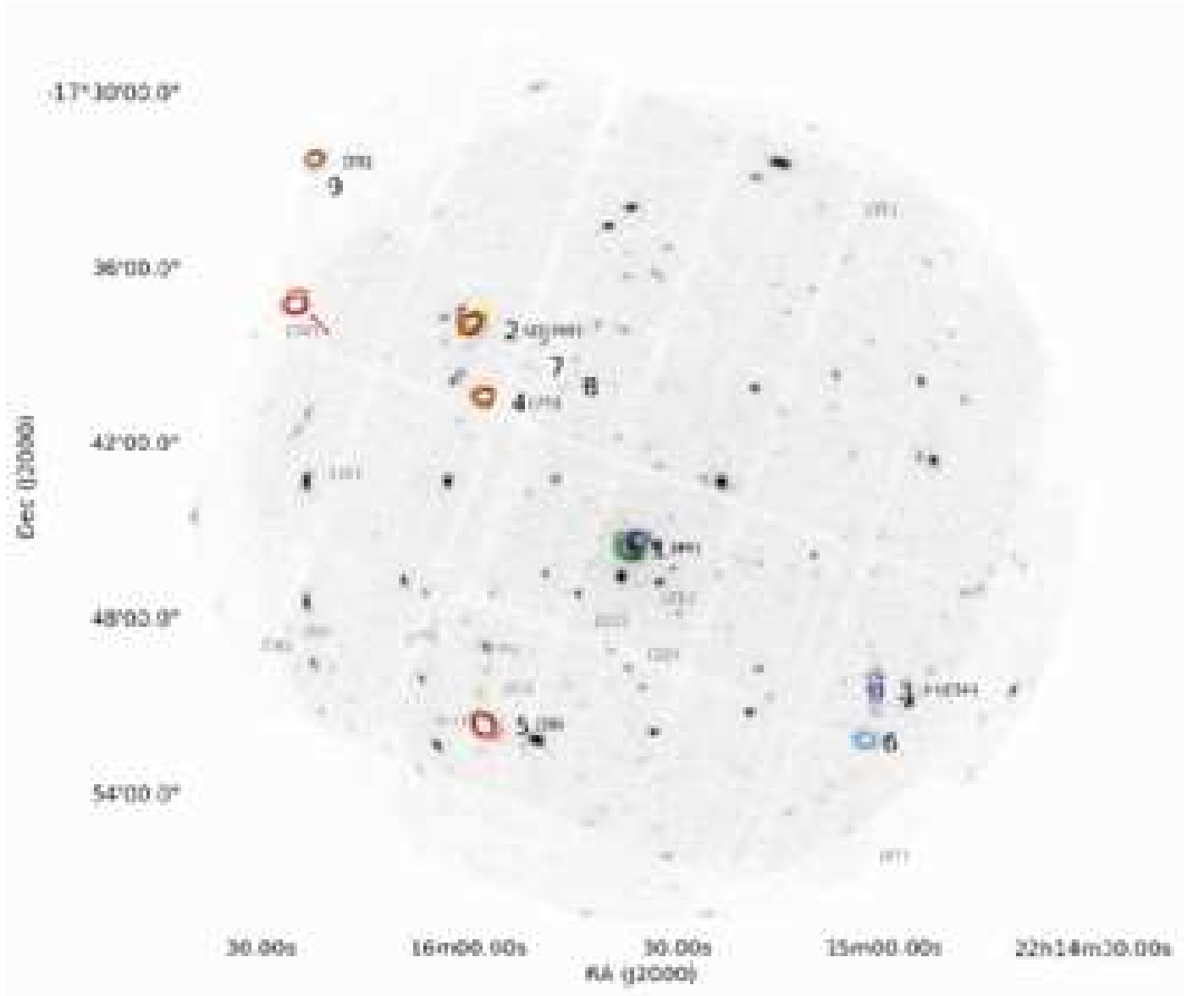


Fig. 4: over-density contours of galaxies within the field of view of the XMM-Newton pointing. The background image is the stacked image of all XMM-Newton observations of LBQS2212 (0.5 – 2.0 keV). The extended X-ray sources from Figure 1 are indicated with their identifiers on the side (1 arcmin offset in R.A.). In smaller fonts the identifiers from other works are indicated either in black, if presented in this work as well, or in grey if not found by our method. Between round brackets the identifier from Bielby et al. (2010) is indicated and square brackets refer to the catalogue from Olsen et al. (2007). Curly brackets present the clusters from Adami et al. (2010). The red arrow points at an optical over-density, which has no clear counterpart in X-rays. The contours represent 5 Poissonian likelihood levels with  $10 < L < L_{max}$ , colour-coded, or rather colour-mapped, by redshift interval: *purple*  $z = 0.3$   $L_{max} = 15$ , *blue*  $z = 0.35$   $L_{max} = 20$ , *green*  $z = 0.45$   $L_{max} = 20$ , *dark pink*  $z = 0.78$   $L_{max} = 30$ , *orange*  $z = 0.98$   $L_{max} = 15$ , *red*  $z = 1.18$   $L_{max} = 20$ , *heat*  $z = 1.38$   $L_{max} = 20$ , where  $z$  refers to  $z_{min} + \frac{1}{2}\Delta z$ , i.e. the middle of the bin.

shift  $z \gtrsim 1.1$ , disregarding all sources at lower redshift. The number density of sources (40 per  $\square^\circ$ ) they find is roughly equal to the results from our search algorithm using XMM-SAS. These authors report on three distant X-ray luminous groups within the area covered in this paper, of which two (see Figure 4) have been retrieved by us as well both as X-ray and optical over-density structures. Interestingly, Bielby et al. (2010) make no reference to the source ext#4, described in Section 5.4. One of their sources, ID-32 or WIRDXC J2216.4-1748, could not be confirmed by us.

Likewise, we have been able to spectroscopically refine the two photometric cluster redshifts found by these authors.

#### 4. Optical spectroscopy

The spectroscopic results used in this publication were obtained with FORS2 mounted on the VLT through observing programme 079.A-0369(C) (Aug./Sept. 2007) and 080.A-0659(A) (Oct./Nov. 2007 and Jun. 2008). The total integration time of roughly 19 hours was used to target the nearby cluster candidates ext#1, ext#3 and ext#6 with three

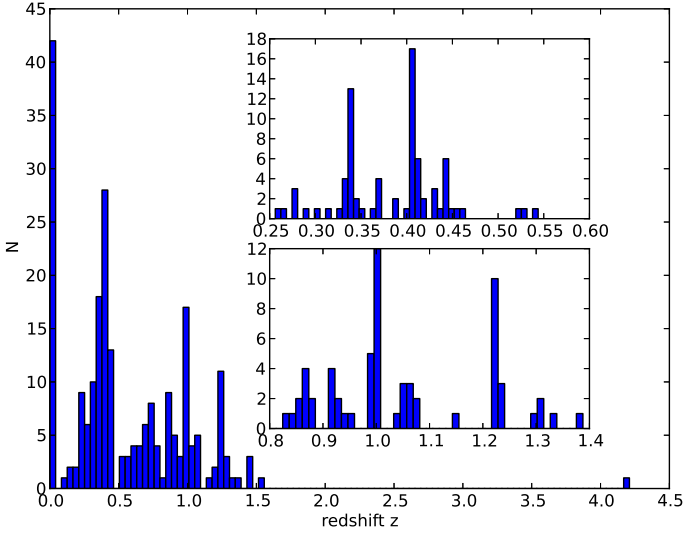


Fig. 5: Histogram of all 231 science grade spectra. The insets show a zoom-in on the low (top) and high (bottom) redshift range.

masks through grism 150I and the distant cluster candidates ext#4 and ext#5 with four masks through grism 300I grism. As spectroscopic targets we prioritised those objects that lie close to the X-ray emission peak and/or have colours close to the red sequence as determined from the ESO-VLT imaging. We also targetted some X-ray point sources.

The science data was flat-fielded and wavelength-calibrated with the appropriate calibration files supplied by the FORS2 database. The bias was read from the chip over-scan region. Flux calibration has been applied with a single response curve derived from only one observation. No atmospheric correction has been performed. The recorded spectra have a spectral coverage from 6 000–10 000 Å ( $\mathcal{R} = 660$ ) and 4 000 – 10 000 Å ( $\mathcal{R} = 260$ ) for the 300I and 150I respectively, where  $\mathcal{R}$  denotes the resolving power.

From 289 slits we were able to extract 231 science-grade spectra, plus 19 double recordings, having sufficient signal-to-noise to classify the spectra and measure redshifts, of which six are QSOs and 42 (late-type) stars. Their redshift distribution is shown in Figure 5. A total of 66 spectra are of cluster members, excluding ten double recordings. The remaining 118 spectra belong to unrelated field galaxies. The complete catalogue can be viewed as *Online material* in Table 5. The list of cluster members is presented in Table 6. Galaxy cluster members have been selected within an redshift interval  $\Delta z \lesssim 0.015$  around the mean redshift within a projected radius of  $\lesssim 1$  Mpc around the X-ray source.

Redshifts were obtained by correlating the spectra with the elliptical and oldest starburst template from Kinney et al. (1996), both with the EZ software (Garilli et al. 2010) for passive galaxies and the **IRAF FXCOR** task for some galaxies with strong emission lines.

Galaxy spectra were processed from 4500 Å up to 10 000 Å, depending on spectral coverage and faulty regions. Regions with strong sky absorption have been masked out. In most case this range samples the following most prominent features: [OII]  $\lambda\lambda 3726, 3729$  emission lines, the CA H+K  $\lambda\lambda 3934, 3969$  absorption lines, the 4 000 Å-break, the

G-band around  $\lambda \sim 4300$ , the hydrogen lines H $\delta$   $\lambda 4102$  and H $\beta$   $\lambda 4861$ , and [OIII]  $\lambda\lambda 4959, 5007$ . Strong emission line galaxies were sampled in a region around the most prominent emission lines. Only the two mentioned templates were used to avoid systematic redshift shifts due to resolution between templates.

No redshift errors are indicated in Table 6, since the variance in redshift resulting from using different templates (i.e. other templates than the two mentioned above) is generally large ( $\sim 0.001$ ) because of the spectral resolution of the instrument, which is limited to  $\delta z \sim 0.01$ . The formal  $1\sigma$  confidence intervals resulting from the  $\chi^2$  template fit, however, are much smaller, typically  $< 0.001$ . For emission line galaxies the errors are smallest and are given by our spectral wavelength calibration ( $\sim 0.1$  Å), which results in  $\delta z \sim 0.00001$ . Line feature centroids can be determined with much higher precision than the instrumental resolving power. In Table 5, however, we merely present the formal  $1\sigma$  errors.

Table 6: Overview of spectroscopic redshifts for all confirmed cluster members with distances from the X-ray centre  $\lesssim 1$  Mpc/  $\lesssim 1.7$  Mpc/  $> 2.5$  Mpc (white/grey/dark grey background). The ID corresponds to the identifiers in Figures 7,13,16,19,22 in as far they appear within the cut-out. The entries are ordered according to their distance to the X-ray emission peak. The last row contains the mean for each column. Formal redshift errors ( $1\sigma$ ) are typically  $< 0.001$  and not listed here. A complete listing of all science-grade spectra can be found in Table 5.

ID	redshift $z$				
	ext#1	ext#3	ext#4	ext#5	ext#6
A	0.407	0.337	0.999	1.237	0.408
B	0.411	0.337	0.996	1.220	0.405
C	0.409	0.335	1.001	1.222	0.408
D	0.408	0.339	1.005	1.226	0.408
E	0.406	0.337	0.992	1.223	0.413
F	0.406	0.335	0.995	1.224	0.406
G	0.410	0.338	1.003	1.229	0.409
H	0.406	0.343	1.000	1.222	0.419
I	0.408	0.337	1.001	1.228	0.410
J	0.409	0.341	0.999	1.225	0.403
K	0.402	0.339	0.998	1.223	0.409
L		0.339	0.999	1.240	0.407
M		0.338	1.001		0.410
N		0.344			0.418
O		0.337			
P		0.336			
mean	0.408	0.338	0.999	1.227	0.410

## 5. Identifications of XMM-Newton cluster candidates

In the deep CFHT imaging six out of the nine extended X-ray sources can be identified with clusters of galaxies. All mentioned redshifts are mean averaged spectroscopically determined redshifts, unless stated otherwise. Table 7 gives the likely identifications with their photometric redshifts if available. Column “redshift X-ray” gives the  $1\sigma$  range of the X-ray spectroscopic redshift estimates derived from  $kT - z$  contours (see Figures ??-??). The cross-reference redshifts listed in column “redshifts publ.” refer to the optically se-



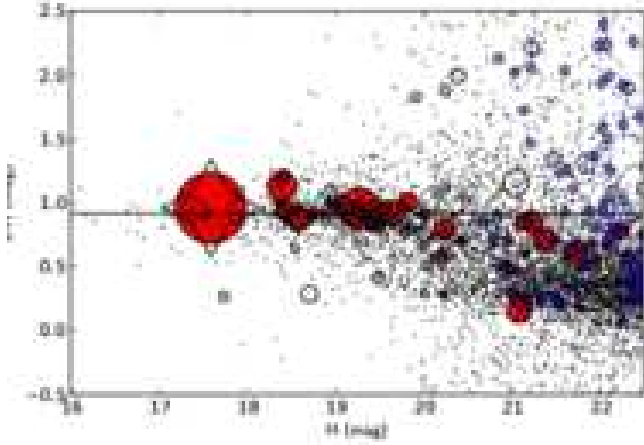


Fig. 6: Colour-magnitude diagram for the extended X-ray source ext#1. CFTHLS D4  $z'$  and  $H$ -band images have been used. The small dots show *all* galaxies within D4 having cluster-concordant photometric redshifts, i.e. within the area between the dashed lines in Fig. 3. Open circles show all galaxies with good photometry  $< 1$  Mpc from the X-ray peak, of which the filled symbols have cluster-concordant photometric redshifts. Vertical dashes indicate the error in the colour. Star symbols indicate spectroscopic members. All symbols (apart from the dots) have been scaled, inversely, to their physical distance from the X-ray emission peak. In each panel, the horizontal line indicates the expected colour of luminous, red sequence galaxies at the given spectroscopic redshift, as obtained from the simple stellar population models calibrated on data available in Fassbender et al. (2011a).

lected catalogues from previous publication. In Figure 6-27 the colour-magnitude diagrams  $H_{\text{mag}}$  vs.  $(z' - H)_{\text{mag}}$  for all X-ray positions are displayed, which are discussed qualitatively for each position individually. The terms *red sequence* and the *expected colour* of a cluster are used invariably, since we assume, as a zeroth-order approximation, a zero gradient of  $z' - H$  (mag) as a function of relative brightness. The values of the empirically determined cluster colour as a function of redshift are taken from Fassbender et al. (2011a). We chose to remain with a single colour, i.e.  $z' - H$ , in order to illustrate its effectiveness thereof for the redshift's range  $0.3 < z < 1.5$  and to be able to relate our results to Fassbender et al. (2011a) (their Fig. 3). Yet, a single colour does not always optimally sample the 4000 Å break, however, the chosen filter combination is a monotonic function of the red sequence of passively evolving galaxies, hence sufficient for our purpose.

### 5.1. XMMU J221536.8-174534 (ext #1) $z = 0.41$

Nearly on axis we find the brightest extended source at a redshift of  $z = 0.408$ . The position of brightest galaxy coincides with the X-ray emission peak, as can be expected for relaxed clusters at relatively low redshifts. The extended X-ray source has been described as a likely cluster of galaxies by Clavel et al. (2006). This is confirmed by our optical imaging. The X-ray spectrum (see Figure ??) is consistent with the photometric redshift  $z = 0.4$  as found in the MF

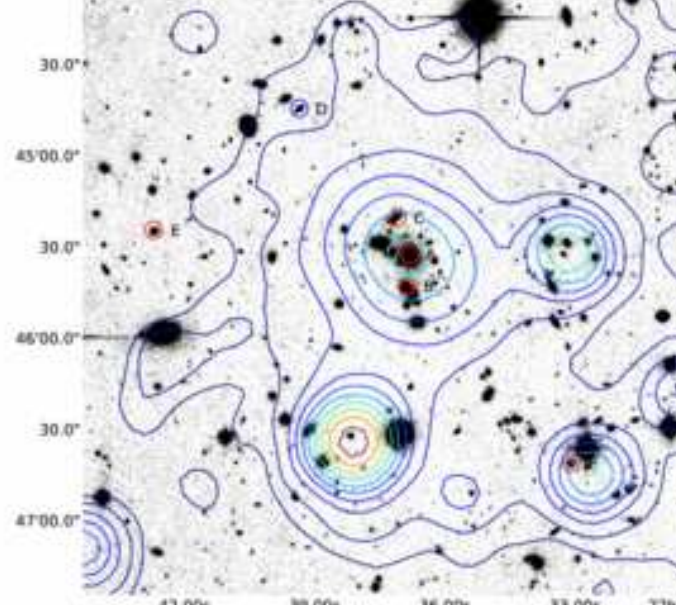


Fig. 7: CFTHLS D4  $z'$ -band image centred on the extended X-ray sources in the field. The blue and red circles indicate the positions of the spectroscopically confirmed star forming and passive cluster members, respectively. The contours overlay represent linearly spaced photon count levels of the X-ray sources. North is up, east is to the right. The image is 1.2 arcmin across.

searches by Olsen et al. (2007) and Dietrich et al. (2007). The CFHT  $z'$ -band image with X-ray contours and spectroscopic members is shown in Figure 7. The cluster has a well-evolved red sequence as seen in Figure 6 consistent with the empirically expected  $z' - H$  colour. Six of its 11 spectra are presented in Figure 8.

In Figure 4 system ext#1 is associated with two over-density contours: the purple ones at  $z \sim 0.3$  and the greens ones at  $z \sim 0.45$ . It is possible, therefore, that the X-ray emission is a superposition of two clusters at different redshifts. From the X-ray redshift-temperature contours and from the positioning of galaxies with respect to the X-ray emission peak, however, we are able to conclude that the X-ray emission originates in the more distant redshift of the two. The structure at  $z \sim 0.3$  was detected only as galaxy over-density and is not regarded as contributing to the X-ray emission. Additionally, we retrieved two spectroscopic redshifts at  $z \sim 0.34$  at about 50 arcsec from the peak of source ext#1, which are listed as object O and P in the ext#3 column in Table 6.

### 5.2. XMMU J221558.6-173810 (ext #2) $z = 1.45$

The most distant galaxy cluster in this field has already been reported by Stanford et al. (2006). It has been the topic of several dedicated studies since then, e.g. studying star formation at high redshift (Hilton et al. 2010; Hayashi et al. 2011). This is one of the most distant known X-ray selected cluster of galaxies with unambiguously strong X-ray emission, albeit with a confirmed contamination from point sources (Hilton et al. 2009). In addition to earlier publications, we find several galaxies with photometric redshifts compatible with  $z \sim 1.45$ . The over-density

Table 7: Optical identifications of extended sources. The column “redshift publ.” lists redshifts from already published works. The last column gives the difference, in percent, between the spectroscopic redshift and the photometric redshift of the BCG.

Seq. #	Source XMMU J..	Identification	Redshift					$\Delta z/(1+z)$ %
			$z_{\text{spec}}$	$z_{\text{phot}}$	$z_{\text{BCG}}$	publ.	X-ray	
1	221536.8-174534	cluster	0.41	0.46	$0.47 \pm 0.05$	$0.4^a, 0.3^d$	0.37-0.4	+3.7
2	221558.6-173810	cluster	-	1.34	$1.37 \pm 0.06$	$1.45^b, 1.37^e, 1.2^a$	0.9-1.6	-4.5
3	221500.9-175038	cluster	0.34	0.29	$0.42 \pm 0.03$	$0.3^a, 0.38^e$	-	-3.4
4	221557.5-174029	cluster	1.00	0.90	$0.98 \pm 0.04$	$0.95^e$	0.9-1.2	-5.0
5	221556.6-175139	cluster	1.23	1.12	$1.23 \pm 0.04$	$1.17^c$	> 0.9	-4.8
6	221503.6-175215	cluster	0.41	0.42	$0.49 \pm 0.06$	-	-	+0.8
7	221546.2-174002	empty field	-	-	-	-	-	-
8	221551.7-173918	empty field	-	-	-	-	-	-
9	221624.3-173321	point source	-	-	-	-	-	-

**References.** <sup>a</sup>Olsen et al. (2007); spectroscopic redshift, <sup>b</sup>Stanford et al. (2006); <sup>c</sup>Bielby et al. (2010); <sup>d</sup>Grove et al. (2009); <sup>e</sup>Adami et al. (2010).

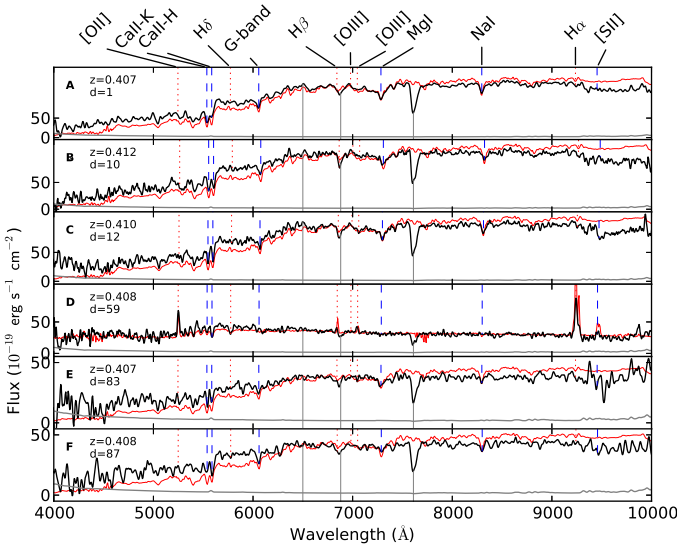


Fig. 8: Selected spectra for cluster ext#1 in the observers’ frame in black and their noise spectra in grey. Either an elliptical or emission template is overplotted in red. The positions of expected absorption and emission features have been indicated with blue dashed and red dotted lines, respectively. Vertical grey lines indicate regions affected by sky absorption. The spectra have been smoothed for clarity. The capital letters correspond to the entries in Table 6 and to the positions in Figure 7. The redshift  $z$  and the distance  $d$  (arcsec) to the formal peak of the X-ray source are indicated in the plot.

contours in Figure 4 for this cluster are displayed with the *heat* colour scheme. An CFHT  $z'$ -band image is shown in Figure 10 with X-ray contour overlays and the positions of three new quasars indicated, of which two reside at the cluster redshift. The colour-magnitude diagram in Figure 9 shows that a red sequence is already present at this high redshift, following the empirically expected colour. We have not obtained additional galaxy spectra in our observation runs.

However, we serendipitously identified two quasars at the nominal cluster redshift on the very outskirts of the cluster (see Figure 10). The spectra are presented in Figure

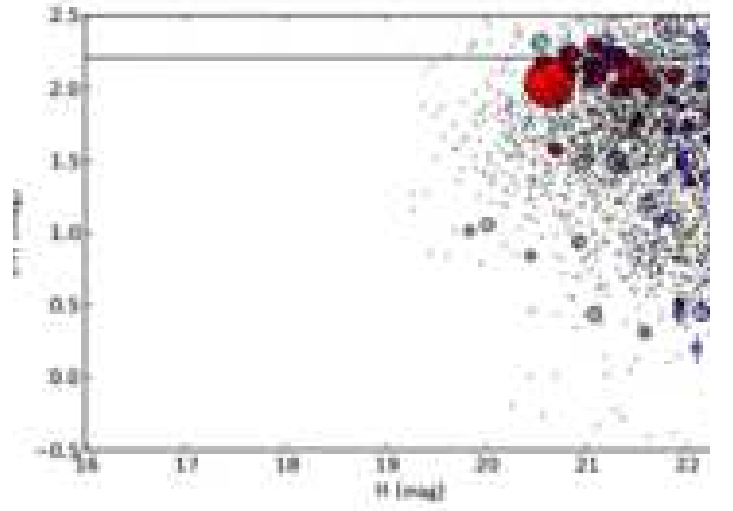


Fig. 9: As in Figure 6 for source ext#2 at  $z = 1.45$ .

11 (identifiers A and B). For future spectroscopic X-ray analysis, these X-ray sources do not need to be included as power laws contributing to the X-ray flux since they lay beyond 1 arcmin, i.e. farther than the spectral extracting radius. In a joint *Chandra*-XMM-Newton analysis, Hilton et al. (2010) report a temperature of 4.1 kT with the inclusion of three power laws to account for point source contributions. In contrast, our analysis, as stated before, assumes the emission to result from only a single hot plasma. The extraction region used by Hilton et al. (2010) is only mildly (7 arcsec) larger than the one we used.

### 5.3. XMMU J221500.9-175038 (ext #3) $z = 0.34$

At a mean redshift  $z = 0.338$  cluster ext#3 is the closest galaxy cluster in the field. This cluster was also detected in the MF searches by Olsen et al. (2007) ( $z \sim 0.3$ ) and Dietrich et al. (2007). We show the CFHT  $z'$ -band image with X-ray emission contours and labelled spectroscopic members in Figure 13. The red sequence is easily visible in Figure 12 at the colour expected for its redshift. Its selected

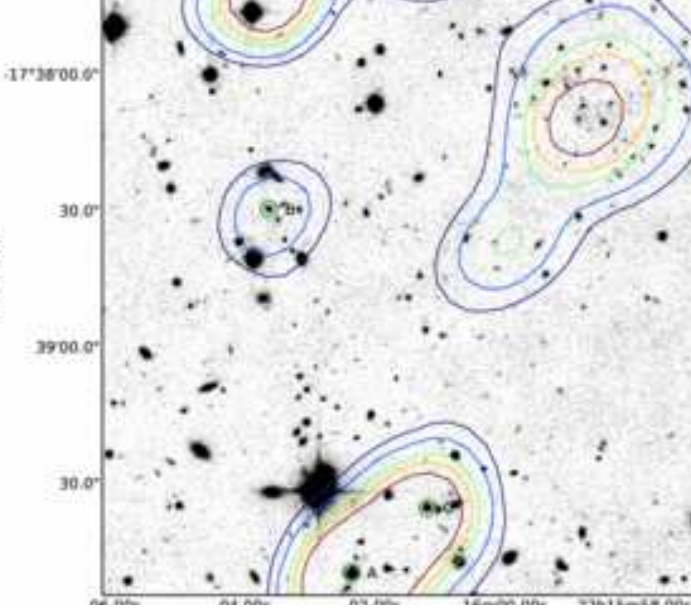


Fig. 10: As in Fig. 7 for source ext#2. The cluster is NE of the image centre. No new spectra have been obtained for this publication, apart from the three labelled X-ray point sources, whose optical spectra are shown in Figure 11.

14 spectroscopic members are within  $|z - z_{\text{cluster}}| \lesssim 0.006$ . Figure 14 shows six of the confirmed members.

In the same redshift bin as cluster ext#3 (green contours in Figure 4) we find an over-density of galaxies virtu-

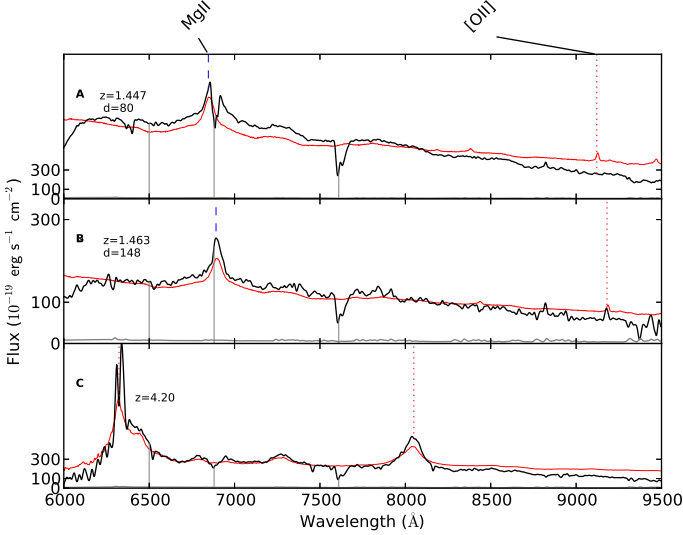


Fig. 11: Spectra (black) of the quasars discovered in the vicinity of cluster ext#2. In red a quasar template is over-plotted. Objects A and B can be regarded as cluster members or rather active galaxies in the cluster outskirts. Object C is an unrelated distant X-ray luminous quasar serendipitously found in this study (Lamer et al. 2011). The labels correspond to the objects identified in Figure 10. Spectral features, etc., are coded as in Figure 8. In the case of A the emission lines are  $\text{Ly}\alpha$  and  $\text{CIV}$ .

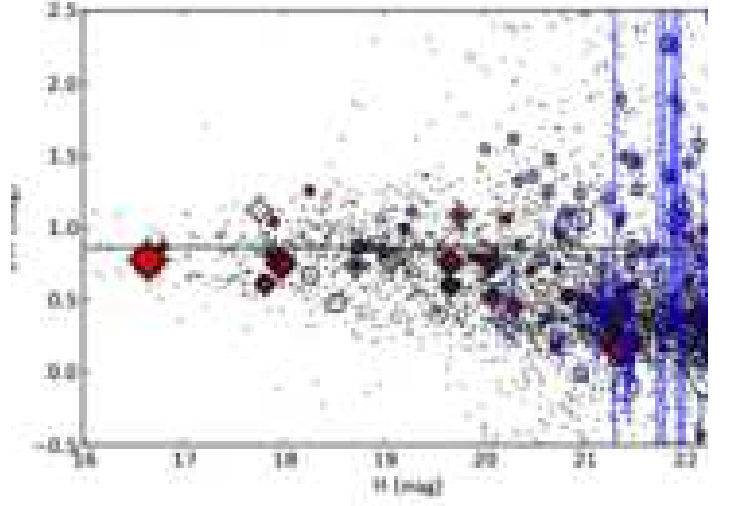


Fig. 12: As in Figure 6 for source ext#3 at  $z = 0.34$

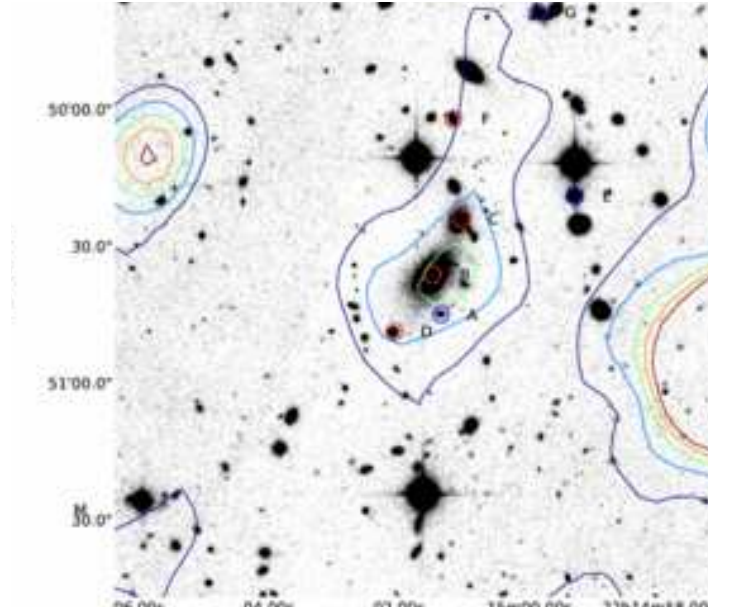


Fig. 13: As in Fig. 7 for source ext#3. The associated optical spectra are found in Figure 14.

ally at the same projected position on the sky as the central cluster ext#1. One interpretation is to consider these over-densities to be a sign of knots in the cosmic web  $\sim 3$  Mpc apart; that is, the two galaxy over-densities are part of the same large-scale structure. There is no X-ray detection from a group of galaxies at  $z = 0.338$  at the coordinates of cluster ext#1. Namely, the X-ray flux is compatible with only coming from source ext#1 as discussed in Section 5.1.

#### 5.4. XMMU J221557.5-174029 (ext #4) $z = 1.00$

On the very edge of the redshift unity barrier we find a new cluster with 13 members. This cluster has already been referred to by Adami et al. (2010) as a photometric cluster candidate; however, it appears in no other catalogue. Two



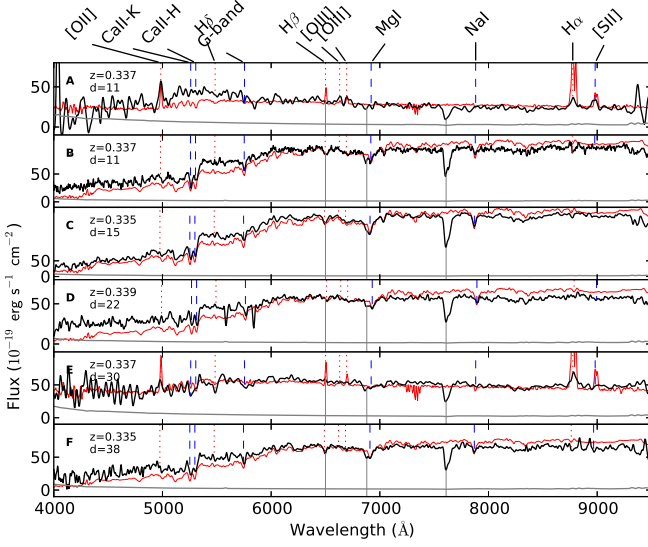


Fig. 14: Selected spectra for cluster ext#3 in the observers' frame. See Fig. 8 for explanation. The positions are seen in Figure 13.

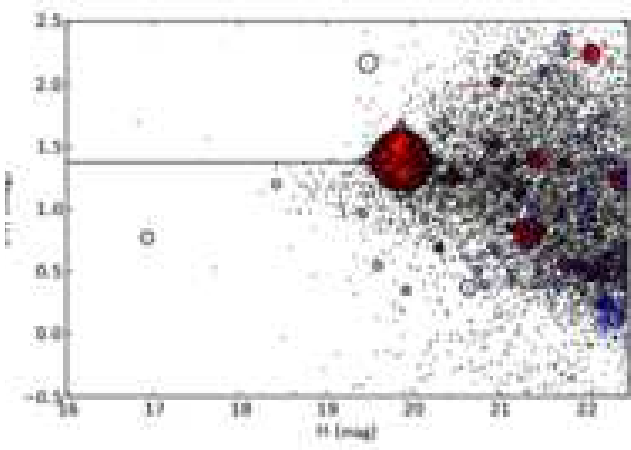


Fig. 15: As in Figure 6 for cluster ext#4 at  $z = 1.00$ .

members are at the very centre of the X-ray emission, and both can be considered BCG, since their fluxes are similar.

The red sequence is visible in Figure 15 without deviations from the expected  $z' - H$  colour. Striking, however is the absence of a clear magnitude gap between the BCGs and the other galaxies, which could indicate a recently formed system. The spectra, a selection of six from 13, are presented in Figure 17. The two BCGs have spectroscopic redshifts  $\Delta z = 0.003$ , which is well beyond their formal ( $1\sigma$ ) errors. The cluster redshift of  $z \sim 1.0$  is consistent with the estimate from the X-ray spectrum. An image of the cluster is shown in Figure 16 with X-ray contours and confirmed members. The apparent point-like morphology of the X-ray emission is purely due to chip gaps masking out the cluster edges.

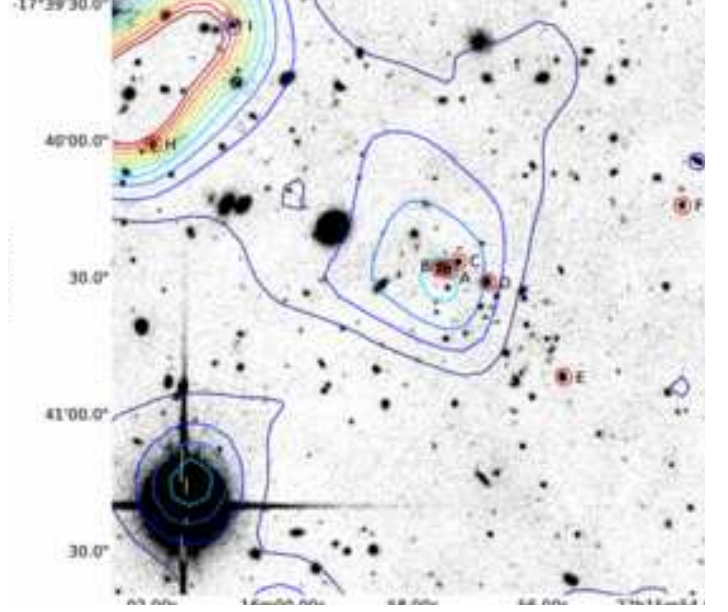


Fig. 16: As in Fig. 7 for source ext#4. The associated optical spectra are found in Figure 17.

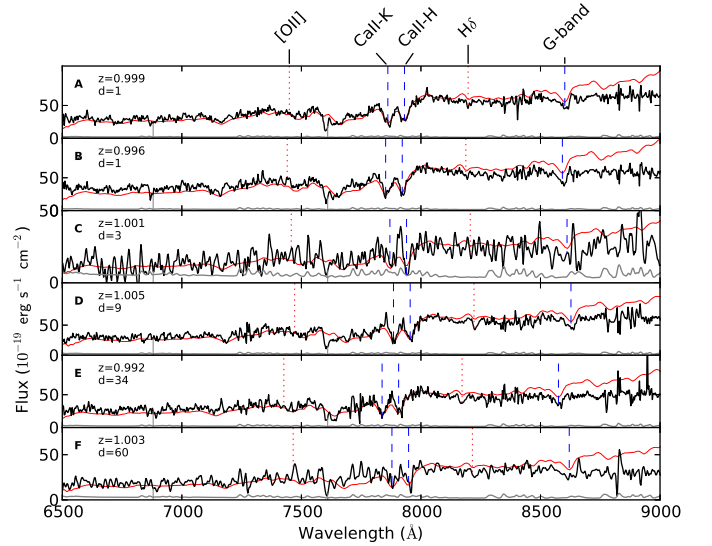


Fig. 17: Selected spectra for cluster ext#4 in the observers' frame. Colours and labels are as in Figure 8. Labels refer to identified objects in Figure 16. The spectra have been smoothed.

##### 5.5. XMMU 221556.6-175139 (ext #5) $z = 1.23$

The optical imaging shows a conglomeration of both nearby and distant galaxies. The CFHT  $z'$ -band image is shown in Figure 19 with X-ray contour and spectroscopically confirmed cluster members. This cluster has already been hinted at by Bielby et al. (2010), however, at a photometric redshift of  $z = 1.17$ . The colour-magnitude of the cluster is somewhat peculiar as seen in Figure 18. The galaxy closest to the X-ray emission peak is blue and star-forming. Its membership is confirmed both spectroscopically and photometrically. Although the colour of the red members is as

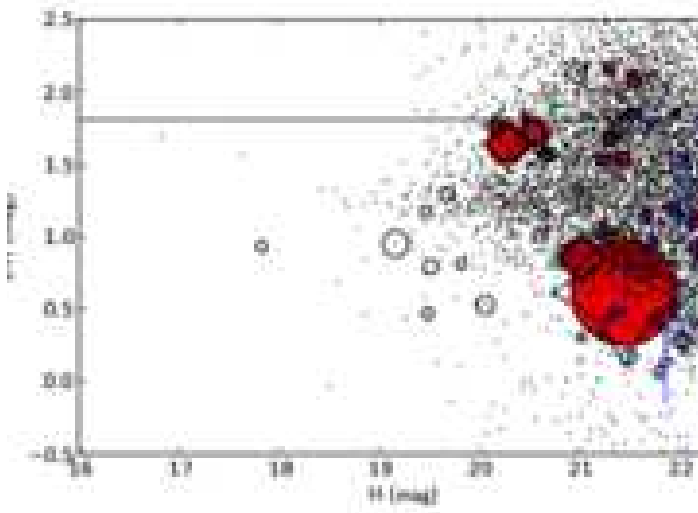


Fig. 18: As in Figure 6 for cluster ext#5 at  $z = 1.23$ .

expected, we note there seems to be a significant ongoing build up of the red sequence. These properties are similar to the cluster found at  $z = 1.56$  by Fassbender et al. (2011b). This second farthest cluster in the field has 12 concordant redshifts with  $|z - z_{\text{cluster}}| \lesssim 0.013$ . Figure 20 shows a selection of six members. Mask offsets<sup>6</sup> during observation caused the signal-to-noise to remain very low. However, due to the existence of single emission lines in the very centre of the clusters, the redshift could be established as  $z = 1.227$ . A redshift based only on one emission line remains tentative; however, the morphology of the galaxy in combination with its extent on the sky does not render it a likely possibility that we are seeing a background high- $z$  Ly $\alpha$  emitter.

<sup>6</sup> Due to accidental pointing errors.

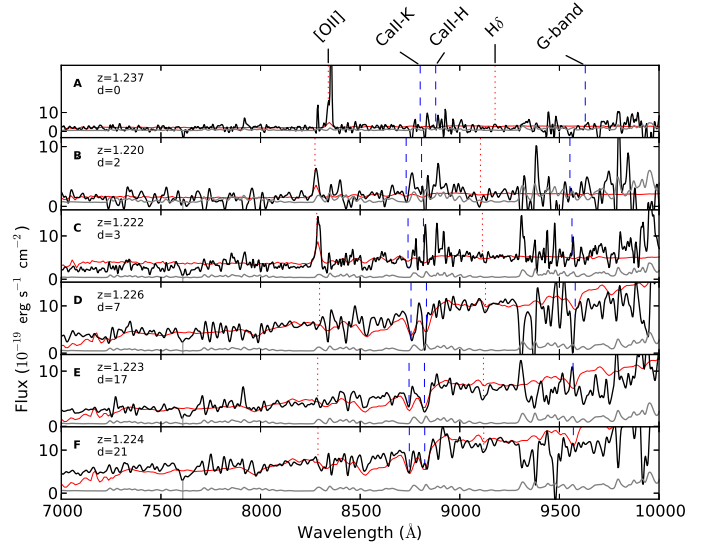


Fig. 20: Selected spectra for cluster ext#5 in the observers' frame. Colours and labels are as in Figure 8. The positions are seen in Figure 19.

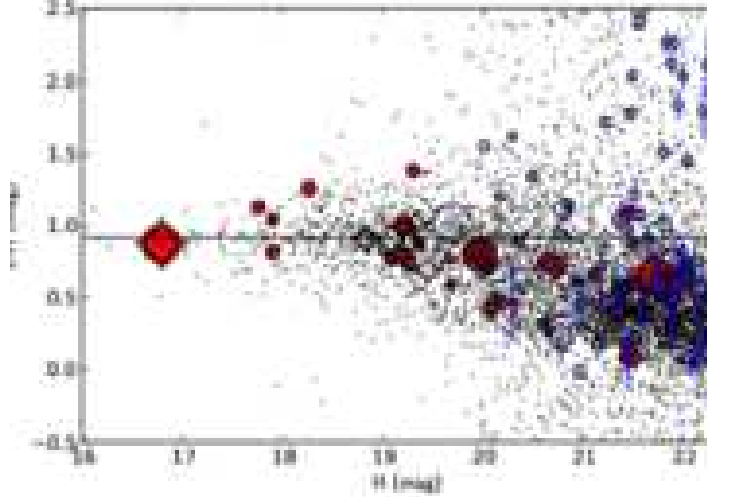


Fig. 21: As in Figure 6 for source ext#6 at  $z = 0.41$ .

For this source the X-ray spectrum indicates a redshift lower limit of  $z > 0.9$ . Both the X-ray and galaxy overdensity contours show an NW-SE elongation.

##### 5.6. XMMU 221503.6-175215 (ext#6) $z = 0.41$

The cluster with the weakest X-ray emission at a redshift of  $z = 0.410$  can easily be understood as a sign of large-scale structure. Cluster ext#6 possibly is a knot in the filaments around the more luminous, hence more massive structure ext #1. This work provides the first reference to this cluster. The colour-magnitude diagram in Figure 21 shows a well-evolved red sequence, which both confirms the maturity of the system and rejects the possibility of a chance alignment. Since the colour is virtually identical to that

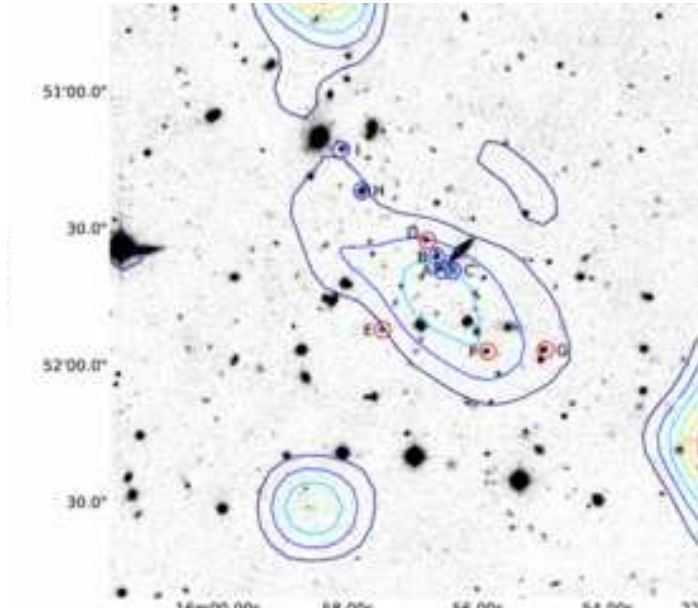


Fig. 19: As in Fig. 7 for source ext#5. The associated spectra are seen in Fig. 20.

of cluster ext#1, we have established further proof for the common redshift of the two clusters. We find 14 spectroscopic members (see Figure 22) for the clusters of which six are plotted in Figure 23.

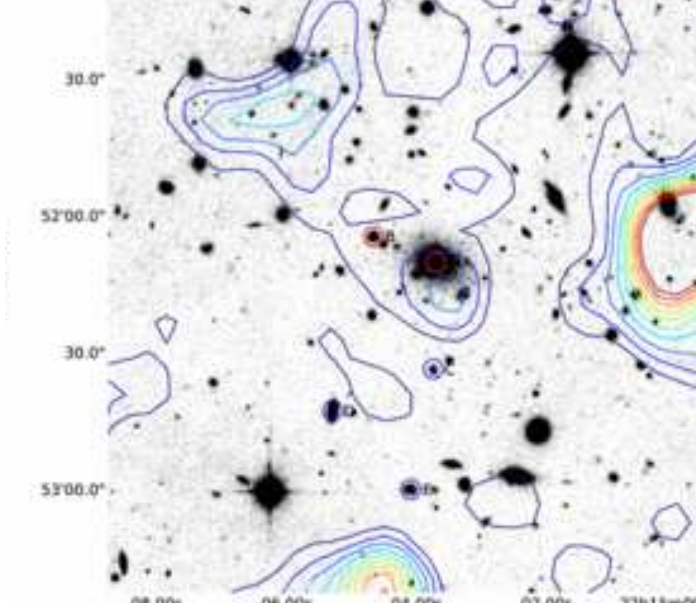


Fig. 22: As in Fig. 7 for source ext#6. The associated spectra are found in Fig. 23.

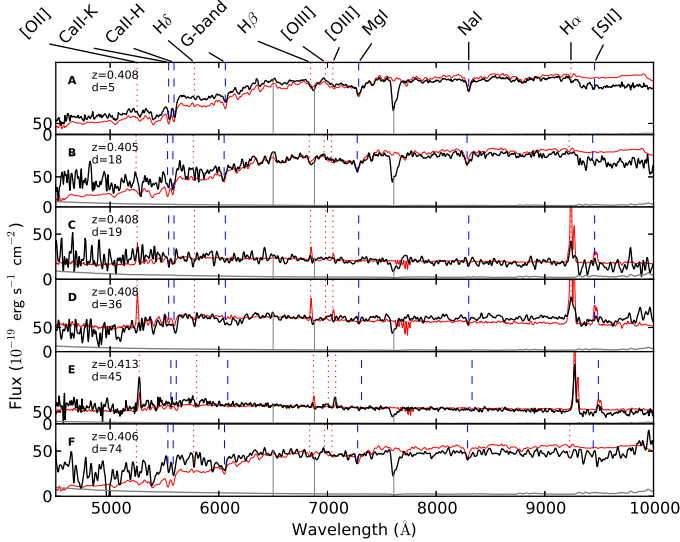


Fig. 23: Selected spectra for cluster ext#6 in the observers' frame. Colours are as in Figure 8. Labels refer to identified objects in Figure 22.

The claim to perceive cluster ext#6 (Figure 4) as part of the larger structure around system ext#1 is supported by the fact that we see emission line galaxies close to the centre of the cluster. Three of the five galaxies nearest to the BCG ( $< 1'$ ) show at least  $H\alpha$  in emission. Evolved clusters are not expected to show strong signs of star formation, yet

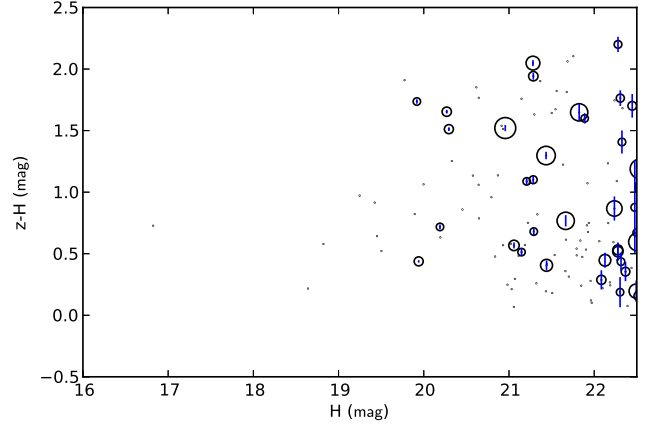


Fig. 24: Colour magnitude diagrams around the two extended X-ray sources (see also Fig. 25) showing no galaxy over-density or obvious red sequence. Open circles denote all galaxies with good photometry within 1 arcmin from the X-ray centroid, scaled inversely with their distance to this centroid. Likewise, the dots represent objects within 2 arcmin.

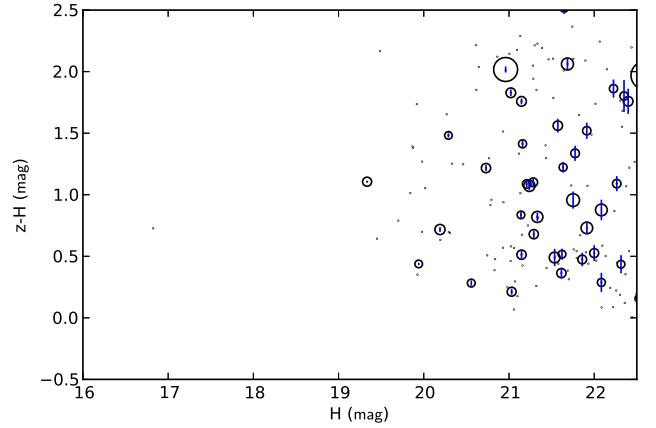


Fig. 25: See caption Fig. 24

in the outskirts of the largest dark matter potentials, such as cluster ext#6, we do expect galaxies to be more active.

### 5.7. XMMU 221546.2-174002 (ext#7) and XMMU 221551.7-173918 (ext#8)

No clear cluster identification for these X-ray sources can be found in the optical data. Their vicinity on the sky makes it is natural to discuss these structures in symbiosis. Remarkably, neither in the very deep CFHT imaging nor in the WIRCam NIR data do we find a plausible visible counterpart for these sources as seen in Fig. 26, which rules out the possibility of a very distant cluster of galaxies within any reasonable redshift limit (i.e.  $z \lesssim 2$ ). The colour-magnitude diagrams as displayed in Figures 24 and 25 do not show any hint of a red sequence.

Source ext#7 has the lowest value for EXT\_LIKE (extent likelihood in Table 3) in this sample and could be a



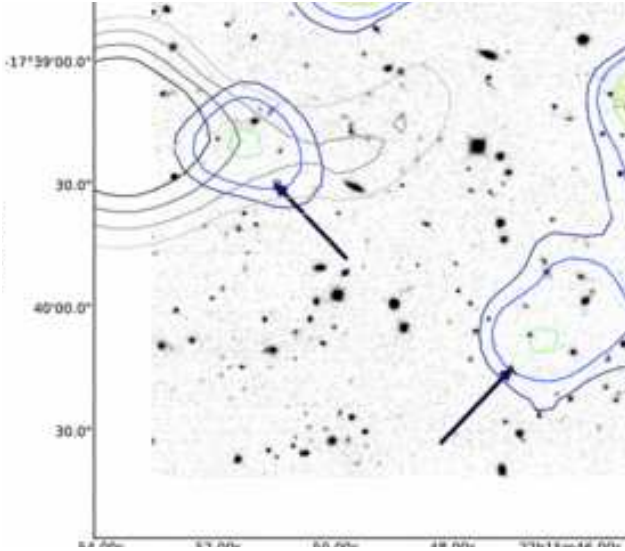


Fig. 26: Source ext#7 and source ext#8. Stack of NIR *HJK* bands to enhance depth for the two unknown structures. Source ext#8 is NW and source ext#7 SE of the image centre as pointed out by the arrows. The grey contours display the NVSS radio source. Dimension and orientation is as in Fig. 7.

blend of faint point sources and/or associated with source ext#8. The NVSS radio catalogue (Condon et al. 1998) contains a faint radio source (3.3 mJy at 1.4 GHz) at 18 arcsecond distance of source ext#8. The projection of the two object on the sky (NW versus SE with respect to the centre of Figure 26) raises the idea of an associated bipolar phenomenon.

Furthermore, that both sources were not detected in the cluster's typical energy band (0.35 – 2.4 keV, see Section 2.1) suggests they may possess a relatively hard spectrum, which in turn favours another mechanism at work rather than bremsstrahlung.

Based on the extended nature of the sources, the radio detection, the hardness of the spectrum, as well as the absence of a clear optical counterpart(s), little alternative is left but to identify source ext#8 (and source ext#7) as a Compton ghost (Fabian et al. 2009).

### 5.8. XMMU 221624.3-173321 (ext#9)

This source is excluded from further (cosmological) analysis, both for its being at a large off-axis angle, namely 16 arcmin (i.e. covered by the EPIC PN camera only), and its likely being a point source. Nonetheless, at about 1 arcmin from source ext#9 there is a complex X-ray structure (at an off-axis angle of 16 arcmin as well), which was not flagged as extended by our source detection. The two sources are displayed in Figure 28, centred on the second source, while source ext#9 is SW towards the bottom. The structure at R.A. 22:16:20.0 Decl. -17:32:25 has also been found by our photometric over-density search. It was proposed that it is at  $z \sim 0.7$  in the MF sample of Olsen et al. (2007) and in the weak lensing sample of Dietrich et al. (2007).

The precise coordinates of the cluster centre (hence the BCG) are problematic to constrain. The position of the X-ray emission peak is not known exactly due to contaminat-

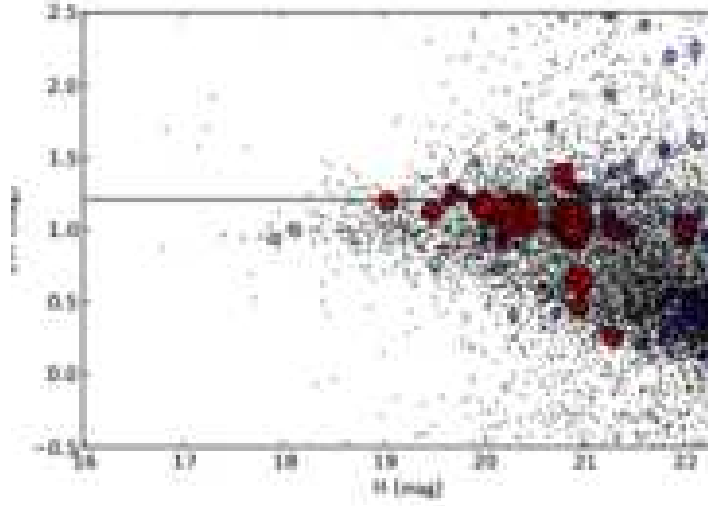


Fig. 27: As in Figure 6 for centre coordinates as described in Section 5.8 close to source ext#9. The difficulty to pin-point the cluster centre results in an only vague red sequence.

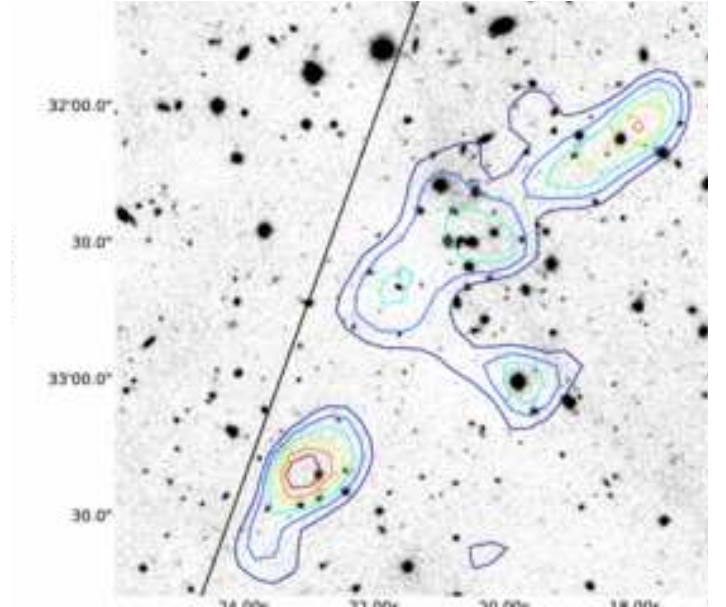


Fig. 28: As in Fig. 7, however, the image is centred on the cluster of galaxies found close to source ext#9 (see Section 5.8). The extended source from our source detection is SE of the image centre. The black line indicates the end of the XMM-Newton EPIC chip.

ing sources and because it is at the very EPIC camera's chip edge. Furthermore, all optical over-density methods have an arcmin-like spatial resolution (see dark pink contours in Figure 4). Therefore, a tentative BCG is selected at  $z = 0.71 \pm 0.07$ , with the need to be confirmed by spectroscopy in the future. The tentative colour-magnitude diagram in Figure 27 is consistent with a redshift of  $z = 0.7$ .

## 6. Cluster counts

### 6.1. X-ray sensitivity function

The advantage of using only X-rays to find clusters of galaxies is the grasp one has on the selection function. In a rather straightforward manner the X-ray behaviour of a cluster sample can be mimicked and convolved with a detector response, thereby obtaining the detection limits for various physical parameters. In this study, the survey completeness is determined using a sensitivity function, which is generated by means of Monte-Carlo simulations. The details of the simulations are presented in Mühlegger (2010) and discussed in Fassbender et al. (2011a). An abbreviated description is found in this section.

The probability of detecting extended X-ray sources at a (1) certain flux limit and (2) a given distance from the optical axis, is computed for ten simulated beta models ( $\beta = \frac{2}{3}$ ) inserted randomly on concentric rings in the stacked XMM-Newton pointings. During insertion, regions that already contain an extended source are avoided. If this were not done, we would introduce an unphysical overlap between clusters at this faint end of the flux scale, which will result in an over-estimation of the source density when correcting for this unrealistic projection effect. The simulated clusters cover a range of 25 bins in both core radii and photon counts. This results in 3125 simulations, since the procedure is repeated five times. The core radii distribution assumed is taken from Vikhlinin et al. (1998). The cluster sample in Vikhlinin et al. (1998) consists of 200 clusters observed with ROSAT with redshift information. The redshifts range from 0.015 – 0.73 with  $z \geq 0.28$ . The advantage of this particular sample is that the core radius is computed by applying  $\beta = 0.67$  as in our analysis. The core radii derived are scaled to how they would appear at  $z = 1$  using the geometrical angular distance dependency on redshift. No further evolution is assumed. The mean core radius at  $z = 1$  is  $\sim 14$  arcsec.

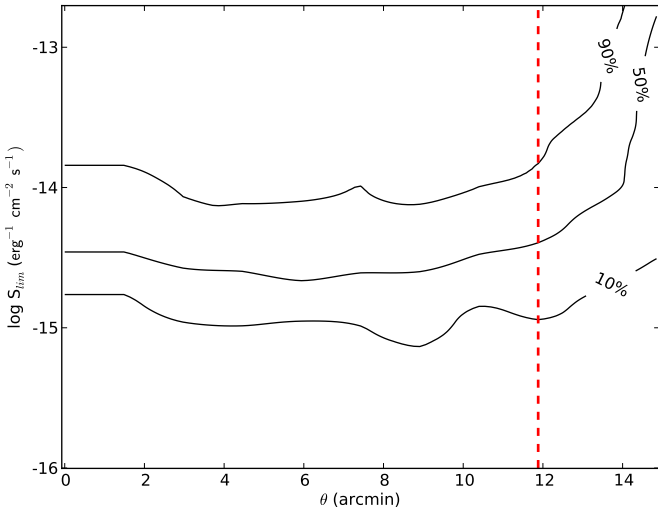


Fig. 29: Survey completeness as a function of off-axis angle and limiting flux. The 10%, 50% and 90% levels are indicated. The dashed red line indicates the restriction put on the off-axis angle.

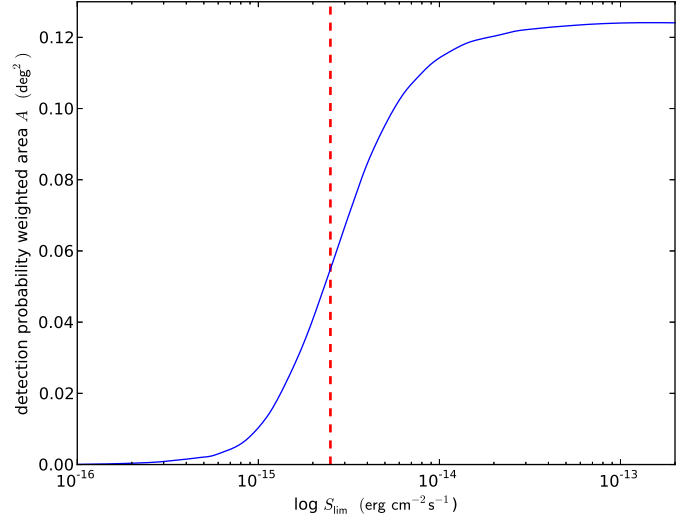


Fig. 30: Cumulatively sensitivity-weighted surface areas as a function of limiting flux, integrated over all off-axis angles. The short-dashed red line indicates the deduced limiting flux of  $2.5 \cdot 10^{-15} \text{ erg cm}^{-2} \text{ s}^{-1}$  at which 50% completeness is reached as indicated in Figure 29.

Source detection is performed for every simulation with XMM-SAS v.6.5 in the multiple energy bands simultaneously with the same parameters as mentioned in Section 2.1. The resulting image displaying the survey completeness level as a function of limiting flux ( $S_{\text{lim}}$ ) and off-axis angle ( $\theta$ ) is shown in Figure 29. We notice that at the indicated completeness levels, the curve is rather flat between ca. 2 – 12 arcmin and in particular the 50% curve, which we take as the completeness level for our survey. Towards the centre of the pointing, however, an extended structure (cluster ext#1) affects the sensitivity in this observation, while on the outskirts the vignetting and the very end of the chip catastrophically affect the detectability of clusters. At the 50% level, corresponding to a flux of  $2.5 \cdot 10^{-15} \text{ erg cm}^{-2} \text{ s}^{-1}$ , we are complete. All clusters detected have (source detection) fluxes above this level. For our  $\log N - \log S$  analysis, none of the objects ext#1-#6 needs to be excluded:

$$A(S_{\text{lim}}) = \sum_{i=1}^{12} \sum_{S_{\text{lim}}} A(\theta_i) \cdot P(\theta_i, S_{\text{lim}}). \quad (10)$$

Dividing the LBQS 2212-1759 observation into rings, we can fold the geometric area with the survey sensitivity at each off-axis angle  $\theta$ . We limit the radius to  $\leq 12$  arcmin. Beyond this radius the sensitivity drops significantly as seen in Figure 29. This area restriction also ensures the coverage by all three EPIC cameras. One extended source (ext#9) is excluded as a result of this angle limit. The cumulative effective surface area, or detection probability weighted area  $A(S_{\text{lim}})$ , computed following equation (10) is displayed in Figure 30. Owing to our limit on the maximum radius, we obtain an survey area of  $\sim 0.13 \text{ deg}^2$ .  $S_{\text{lim}}$  denotes the limiting flux. This is the correction curve to be convolved with the clusters' number counts in the purely geometrical survey area, resulting in the survey-independent cosmological cluster count in flux bins.

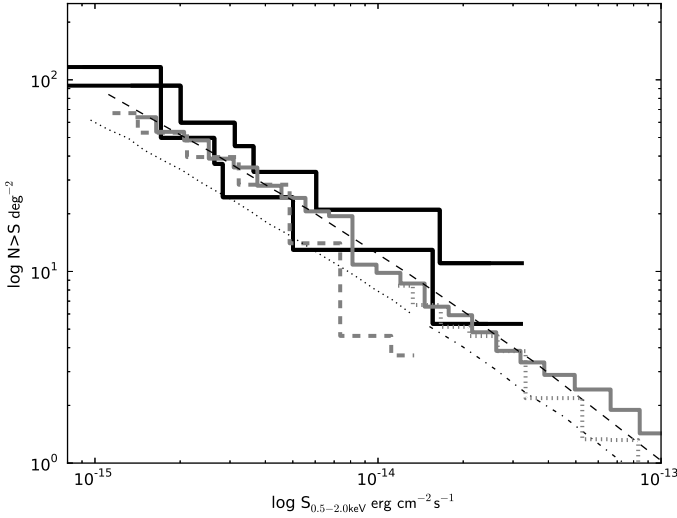


Fig. 31: Cosmological  $\log N - \log S$  for clusters of galaxies. The black discrete curve shows the confidence interval resulting from measured source detection flux errors and an additional  $\sqrt{N}$  on the number count from this work. A comparison to comparable surveys is made. The curves show the model from Rosati et al. (2002) for no evolution (dashed). The dot-dashed and dotted lines show the measured ROSAT brightest cluster sample (BCS, Ebeling et al. 1998) clusters and their extrapolation, respectively. The discrete lines display the findings from COSMOS (solid) (Finoguenov et al. 2007), SXDF (dashed) (Finoguenov et al. 2010), and XMM-BCS (dotted) (Suhada et al. 2012).

## 6.2. $\log N - \log S$

The computed sensitivity function is used to predict the number of X-ray luminous clusters in a certain survey area. We convolve the probability of detecting clusters in concentric rings around the focal axis with the enclosed area (Figure 30). The observed flux distribution is normalised to the probability weighted survey area to obtain the expected number of galaxy clusters per flux bin. The  $\log N - \log S$  graph is presented in Figure 31. The empirical values are compared to the expected numbers simulated by Rosati et al. (2002, 1998), which in turn proved to be a good approximation for the extended X-ray source distribution in the COSMOS (Finoguenov et al. 2007) and the Subaru-XMM-Newton deep field (SXDF, Finoguenov et al. 2010).

When making the link between the derived flux limits and our measured fluxes, we have to bear in mind that the simulated clusters cover a range of core radii as they appear at  $z = 1$ . Therefore we compute  $S_{500}$  for hypothetical clusters at  $z = 1$  with  $r_c = 14$  arcsec, using the iterative approach, which spans the flux range from our simulations. The mean conversion factor between  $S_{\text{lim}}$  and  $S_{500}$  is 0.8, which we apply to our limiting fluxes.

The intrinsic errors resulting from the method used to obtain  $S_{500}$  do not enter into Figure 31, but only the spectral flux errors. Furthermore, since the distribution of clusters on the sky is Poissonian, we add an additional error of  $\sqrt{N}$  on the number counts.

The number counts in flux bins from this study are, among others and within errors, compatible with the findings from the SXDF and COSMOS. Likewise, using spectral or source detection fluxes has no dramatic effect on the results. For low-flux objects, the scenario in which there is *no evolution* in the XLF for extended sources (Rosati et al. 2002) is favoured.

## 7. Summary

This work presents the detection and study of extended X-ray sources in a deep (250 ksec) XMM-Newton field covering a field of view of  $\sim 14$  arcmin across. The nature of the sources has been identified. We have valiantly achieved “five at one blow”, since this single field has allowed us to discover five new spectroscopically confirmed clusters. In the following we summarise the most essential findings from this study.

- We performed a robust source detection on deep, stacked XMM-Newton observations targetting LBQS 2212-1759, revealing nine extended sources with conservative detection thresholds. Six of these sources prove to be clusters of galaxies, five of which are new spectroscopically confirmed discoveries from this work alone. The sixth detected cluster was already known from Stanford et al. (2006). The first unconfirmed extended source, at  $> 14$  arcmin off-axis, is a confused point source. The remaining two sources could not be identified. Since the detection of these sources is dominated by the hard energy bands, this suggests that another mechanism than bremsstrahlung is responsible for the X-ray emission from these two sources, which possibly leads at least one of them to be a Compton ghost.
- A complementary qualitative optical/IR completeness study, allowed by very deep CFHTLS data (i.e.  $z'_{\text{lim}} = 26.0$   $H_{\text{lim}} = 24.6$ ), has confirmed that all X-ray luminous clusters to be associated with an optical over-density, in agreement with the spectroscopic redshift. One new, significant over-density could not be correlated with any X-ray emission, hinting at a projection effect in the optical search method.
- The X-ray selection function has been computed through extensive Monte-Carlo simulations. The approach of retrieving generated  $\beta$  models inserted into the observations has given us a 50% completeness flux limit of  $\sim 2.5 \cdot 10^{-15} \text{ erg s}^{-1}$  over most of the field of view. We constructed a  $\log N - \log S$  based on a complete sample of spectroscopically confirmed sources down to weak fluxes in a precisely determined survey area with a known selection function. Our result agrees with the findings from the COSMOS and the SXDF. Comparing the number counts with the models from Rosati et al. (2002), our data seems to favour no evolution in the XLF in the faint flux range we covered.
- By spectroscopic follow-up of some X-ray point sources, we serendipitously discovered three new AGN. Two of these objects reside at the concordant redshift of the cluster (Stanford et al. 2006) at  $z = 1.45$ . The other quasar has a redshift of  $z = 4.20$ , so is among the handful of most distant X-ray-selected AGN known today (Fiore et al. 2012).

In this deep field study, good photometric data have allowed us to scan the sky in multiple wavelengths to study

the galaxy counterparts of extended X-ray emission. We emphasise that photometric redshifts with errors  $\Delta z < 0.1$  are still too expensive to date for routinely performing this kind of analysis. With respect to the upcoming X-ray mission eROSITA (Predehl et al. 2011), future optical surveys such as LSST (Ivezic et al. 2008), the ESO/Vista project VHS (Arnaboldi et al. 2007)<sup>7</sup>, and PanStarrs (Kaiser et al. 2002) will obtain sufficient depth and cover enough area to identify a wide range of distant and faint X-ray clusters. This work, therefore, could very well be extended to a much larger area of the sky within the next decade.

In the near future, as the photometric and spectroscopic follow-up campaigns for the XDCP is becoming complete, we are already compiling catalogues of distant clusters to extend the present work.

*Acknowledgements.* AdH was supported by the DFG under fund no. Schw536/24-2. GL acknowledges support by the Deutsches Zentrum für Luft- und Raumfahrt (DLR) under contract no. FKZ 50 OX 0201 and 50 QR 0802.

JPD is supported by the German Science Foundation (DFG) through the Transregio 33 and the Cluster of Excellence “Origin and Structure of the Universe”, funded by the Excellence Initiative of the Federal Government of Germany, EXC project number 153.

DP acknowledges the kind hospitality at the MPE.

This research made use of (1) APLpy, an open-source plotting package for Python hosted at <http://aplpy.github.com> and (2) IPython, an interactive python shell (Pérez & Granger 2007).

We are grateful to the CFHT survey team for conducting the observations and the TERAPIX team for developing software used in this study. We acknowledge use of the Canadian Astronomy Data Centre, which is operated by the Dominion Astrophysical Observatory for the National Research Council of Canada’s Herzberg Institute of Astrophysics. It is based on observations obtained with WIRCam, a joint project of CFHT, Taiwan, Korea, Canada, France, at the Canada-France-Hawaii Telescope (CFHT) which is operated by the National Research Council (NRC) of Canada, the Institut National des Sciences de l’Univers of the Centre National de la Recherche Scientifique of France, and the University of Hawaii. This work is based in part on data products produced at TERAPIX, the WIRDS (WIRCam Deep Survey) consortium, and the Canadian Astronomy Data Centre. This research was supported by a grant from the Agence Nationale de la Recherche ANR-07-BLAN-0228. This research has made use of the NASA/IPAC Extragalactic Database (NED), which is operated by the Jet Propulsion Laboratory, California Institute of Technology, under contract with the National Aeronautics and Space Administration.

M. L. thanks the European Community for the Marie Curie research training network “DUEL” doctoral fellowship MRTN-CT-2006-036133.

## References

Adami, C., Durret, F., Benoist, C., et al. 2010, *A&A*, 509, A81  
 Andreon, S., Maughan, B., Trinchieri, G., & Kurk, J. 2009, *A&A*, 507, 147  
 Arnaboldi, M., Neeser, M. J., Parker, L. C., et al. 2007, *The Messenger*, 127, 28  
 Bender, R., Appenzeller, I., Böhm, A., et al. 2001, in *Deep Fields*, ed. S. Cristiani, A. Renzini, & R. E. Williams, 96  
 Bertin, E. & Arnouts, S. 1996, *A&AS*, 117, 393  
 Bielby, R. M., Finoguenov, A., Tanaka, M., et al. 2010, *A&A*, 523, A66  
 Böhringer, H., Mullis, C., Rosati, P., et al. 2005, *The Messenger*, 120, 33  
 Böhringer, H., Schuecker, P., Guzzo, L., et al. 2004, *A&A*, 425, 367  
 Brimiouille, F., Lerchster, M., Seitz, S., Bender, R., & Snigula, J. 2008, *ArXiv e-prints*  
 Cash, W. 1979, *ApJ*, 228, 939  
 Clavel, J., Schartel, N., & Tomas, L. 2006, *A&A*, 446, 439

Condon, J. J., Cotton, W. D., Greisen, E. W., et al. 1998, *AJ*, 115, 1693  
 Coupon, J., Ilbert, O., Kilbinger, M., et al. 2009, *A&A*, 500, 981  
 Dietrich, J. P., Erben, T., Lamer, G., et al. 2007, *A&A*, 470, 821  
 Dietrich, J. P., Miralles, J.-M., Olsen, L. F., et al. 2006, *A&A*, 449, 837  
 Ebeling, H., Edge, A. C., Böhringer, H., et al. 1998, *MNRAS*, 301, 881  
 Erben, T., Hildebrandt, H., Lerchster, M., et al. 2009, *A&A*, 493, 1197  
 Fabian, A. C., Chapman, S., Casey, C. M., Bauer, F., & Blundell, K. M. 2009, *MNRAS*, 395, L67  
 Fassbender, R., Böhringer, H., Nastasi, A., et al. 2011a, *New Journal of Physics*, 13, 125014  
 Fassbender, R., Nastasi, A., Böhringer, H., et al. 2011b, *A&A*, 527, L10  
 Finoguenov, A., Guzzo, L., Hasinger, G., et al. 2007, *ApJS*, 172, 182  
 Finoguenov, A., Watson, M. G., Tanaka, M., et al. 2010, *MNRAS*, 403, 2063  
 Fiore, F., Puccetti, S., Grazian, A., et al. 2012, *A&A*, 537, A16  
 Garilli, B., Fumana, M., Franzetti, P., et al. 2010, *PASP*, 122, 827  
 Gavazzi, R. & Soucail, G. 2007, *A&A*, 462, 459  
 Gobat, R., Daddi, E., Onodera, M., et al. 2011, *A&A*, 526, A133  
 Grove, L. F., Benoist, C., & Martel, F. 2009, *A&A*, 494, 845  
 Hayashi, M., Kodama, T., Koyama, Y., Tadaki, K.-I., & Tanaka, I. 2011, *MNRAS*, 415, 2670  
 Henry, J. P., Salvato, M., Finoguenov, A., et al. 2010, *ApJ*, 725, 615  
 Hilton, M., Lloyd-Davies, E., Stanford, S. A., et al. 2010, *ApJ*, 718, 133  
 Hilton, M., Stanford, S. A., Stott, J. P., et al. 2009, *ApJ*, 697, 436  
 Ilbert, O., Arnouts, S., McCracken, H. J., et al. 2006, *A&A*, 457, 841  
 Ivezic, Z., Tyson, J. A., Acosta, E., et al. 2008, *ArXiv e-prints*  
 Kaiser, N., Aussel, H., Burke, B. E., et al. 2002, in *Society of Photo-Optical Instrumentation Engineers (SPIE) Conference Series*, Vol. 4836, *Society of Photo-Optical Instrumentation Engineers (SPIE) Conference Series*, ed. J. A. Tyson & S. Wolff, 154–164  
 Kinney, A. L., Calzetti, D., Bohlin, R. C., et al. 1996, *ApJ*, 467, 38  
 Lamer, G., de Hoon, A., Fassbender, R., et al. 2011, in *The X-ray Universe 2011*, ed. J.-U. Ness & M. Ehle, 239  
 Lamer, G., Schwöpe, A., Böhringer, H., et al. 2006, in *ESA Special Publication*, Vol. 604, *The X-ray Universe 2005*, ed. A. Wilson, 729  
 Lerchster, M., Seitz, S., Brimiouille, F., et al. 2011, *MNRAS*, 411, 2667  
 Lloyd-Davies, E. J., Romer, A. K., Mehrtens, N., et al. 2011, *MNRAS*, 418, 14  
 Mignano, A., Miralles, J.-M., da Costa, L., et al. 2007, *A&A*, 462, 553  
 Mühlegger, M. 2010, PhD thesis, Technischen Universität München  
 Mullis, C. R., Rosati, P., Lamer, G., et al. 2005, *ApJ*, 623, L85  
 Nastasi, A., Fassbender, R., Böhringer, H., et al. 2011, *A&A*, 532, L6  
 Olsen, L. F., Benoist, C., Cappi, A., et al. 2007, *A&A*, 461, 81  
 Papovich, C., Momcheva, I., Willmer, C. N. A., et al. 2010, *ApJ*, 716, 1503  
 Pérez, F. & Granger, B. E. 2007, *Comput. Sci. Eng.*, 9, 21  
 Pierre, M., Clerc, N., Maughan, B., et al. 2011, *ArXiv e-prints*  
 Postman, M., Lubin, L. M., Gunn, J. E., et al. 1996, *AJ*, 111, 615  
 Predehl, P., Andritschke, R., Becker, W., et al. 2011, in *Society of Photo-Optical Instrumentation Engineers (SPIE) Conference Series*, Vol. 8145, *Society of Photo-Optical Instrumentation Engineers (SPIE) Conference Series*  
 Reichert, A., Böhringer, H., Fassbender, R., & Mühlegger, M. 2011, *A&A*, 535, A4  
 Rosati, P., Borgani, S., & Norman, C. 2002, *ARA&A*, 40, 539  
 Rosati, P., della Ceca, R., Norman, C., & Giacconi, R. 1998, *ApJ*, 492, L21  
 Santos, J. S., Fassbender, R., Nastasi, A., et al. 2011, *A&A*, 531, L15  
 Schwöpe, A. D., Lamer, G., Burke, D., et al. 2004, *Advances in Space Research*, 34, 2604  
 Stanford, S. A., Brodwin, M., Gonzalez, A. H., et al. 2012, *ApJ*, 753, 164  
 Stanford, S. A., Romer, A. K., Sabirli, K., et al. 2006, *ApJ*, 646, L13  
 Takey, A., Schwöpe, A., & Lamer, G. 2011, *A&A*, 534, A120  
 Tanaka, M., Finoguenov, A., & Ueda, Y. 2010, *ApJ*, 716, L152  
 Šuhada, R., Song, J., Böhringer, H., et al. 2012, *A&A*, 537, A39  
 Vikhlinin, A., Burenin, R. A., Ebeling, H., et al. 2009, *ApJ*, 692, 1033  
 Vikhlinin, A., McNamara, B. R., Forman, W., et al. 1998, *ApJ*, 502, 558  
 Watson, M. G., Schröder, A. C., Fyfe, D., et al. 2009, *A&A*, 493, 339

<sup>7</sup> data sharing agreement with DES (Dark Energy Survey)

Table 2: Source list of all point sources from source detection on the stacked image generated by `emldetect` as described in Section 2.1. CTS stands for source photon counts and LIKE for detection likelihood.

id	XMMU J	RA (J2000)	DEC (J2000)	CTS	CTS_ERR	RATE $\text{s}^{-1}$	RATE_ERR $\text{s}^{-1}$	FLUX $\text{erg s}^{-1} \text{cm}^{-2}$	FLUX_ERR $\text{erg s}^{-1} \text{cm}^{-2}$	LIKE
1	221515.1-173223	333.812949	-17.539982	7645.99	97.58	9.9986E-02	1.3507E-03	4.8201E-14	8.5430E-16	14945.55
2	221550.2-175208	333.959505	-17.869012	6273.23	89.97	5.6898E-02	8.4996E-04	3.0027E-14	5.6725E-16	10794.41
3	221523.5-174320	333.848141	-17.722276	6395.81	92.54	3.4883E-02	5.1476E-04	1.7462E-14	3.4513E-16	10113.04
4	221623.3-174317	334.097443	-17.721391	5083.60	82.01	7.1080E-02	1.2148E-03	3.9088E-14	7.9878E-16	7965.78
5	221538.1-174632	333.908757	-17.775786	5224.04	86.57	2.9116E-02	4.9236E-04	1.5173E-14	3.3547E-16	7164.72
6	221603.0-174317	334.012692	-17.721537	3028.87	66.49	2.5590E-02	5.8388E-04	1.3759E-14	3.8529E-16	3734.52
7	221456.6-175052	333.735954	-17.847859	2744.57	63.78	2.7092E-02	6.7580E-04	1.4845E-14	4.3134E-16	3429.88
8	221623.4-174724	334.097609	-17.790097	3050.53	66.61	4.4460E-02	1.0397E-03	2.3940E-14	6.6403E-16	3669.26
9	221453.1-174234	333.721286	-17.709666	2713.64	64.34	2.3620E-02	5.8619E-04	1.3016E-14	3.9009E-16	3073.43
10	221604.6-175218	334.019220	-17.871902	2313.78	59.55	2.6474E-02	7.2932E-04	1.4215E-14	4.6594E-16	2573.39
11	221441.6-175026	333.673374	-17.840688	2014.11	53.15	2.0195E-02	5.6507E-04	2.7868E-14	9.3224E-16	2724.19
12	221536.5-173355	333.902317	-17.565446	2395.37	60.56	2.7025E-02	7.3340E-04	1.4424E-14	4.5915E-16	2547.66
13	221609.3-174641	334.039041	-17.778169	1981.41	56.27	2.1148E-02	6.2763E-04	1.0895E-14	4.1226E-16	2203.82
14	221519.4-175111	333.830919	-17.853279	1975.06	58.16	1.7354E-02	5.3837E-04	9.3377E-15	3.4014E-16	1976.91
15	221533.1-174531	333.887995	-17.758715	1919.42	60.32	1.0037E-02	3.2233E-04	5.5306E-15	2.2334E-16	1386.16
16	221601.0-173723	334.004526	-17.623294	1672.92	53.63	1.9995E-02	6.9166E-04	9.9653E-15	4.0875E-16	1571.91
17	221533.3-175152	333.889118	-17.864686	1580.42	51.69	1.3834E-02	4.9006E-04	7.3948E-15	3.0357E-16	1493.37
18	221532.6-174643	333.886063	-17.778808	1784.57	57.18	9.7418E-03	3.1773E-04	5.1909E-15	2.1211E-16	1388.31
19	221602.2-173950	334.009341	-17.664162	1454.34	51.81	1.4391E-02	5.4097E-04	7.5529E-15	3.3917E-16	1047.00
20	221601.0-173936	334.004524	-17.660122	930.03	45.32	8.8275E-03	4.5986E-04	4.6696E-15	2.9017E-16	468.51
21	221539.8-173432	333.916062	-17.575747	1511.04	50.45	1.8033E-02	6.5613E-04	9.6059E-15	3.9655E-16	1338.62
22	221454.8-173952	333.728476	-17.664527	1654.20	53.93	1.7465E-02	6.5181E-04	1.1192E-14	4.2370E-16	1543.49
23	221518.7-174005	333.828296	-17.668236	1241.43	47.26	8.0472E-03	3.1834E-04	4.8904E-15	2.1627E-16	1020.66
24	221639.5-174427	334.164796	-17.741107	949.37	37.18	2.3005E-02	9.6215E-04	1.8114E-14	9.6571E-16	1130.48
25	221622.2-174931	334.092794	-17.825520	1267.40	48.23	1.8652E-02	7.9113E-04	1.0866E-14	4.8383E-16	963.42
26	221557.6-174856	333.990099	-17.815648	1102.16	45.89	9.0653E-03	4.0176E-04	5.3056E-15	2.6006E-16	815.92
27	221550.3-172948	333.959589	-17.496738	1076.21	40.99	2.5989E-02	1.0606E-03	2.1886E-14	1.0784E-15	1131.55
28	221531.7-175610	333.882286	-17.936114	1115.41	45.27	1.3799E-02	6.3757E-04	7.2199E-15	3.6553E-16	831.14
29	221606.7-175001	334.028322	-17.833742	1070.18	44.33	1.1689E-02	5.2671E-04	6.9034E-15	3.3106E-16	855.55
30	221455.2-174226	333.730023	-17.707229	1038.50	45.18	8.7657E-03	4.0784E-04	4.5696E-15	2.5246E-16	649.95
31	221603.5-173742	334.014642	-17.628420	1095.96	46.28	1.2632E-02	5.7958E-04	5.7529E-15	3.3152E-16	734.48
32	221518.5-173254	333.827292	-17.548388	1026.92	44.82	1.2893E-02	6.2476E-04	7.5872E-15	3.7989E-16	671.01
33	221544.4-174707	333.935147	-17.785362	1041.01	45.44	8.0954E-03	4.0272E-04	4.2864E-15	2.3665E-16	684.86
34	221518.2-174942	333.825943	-17.828410	1049.65	44.76	6.9383E-03	3.0710E-04	3.5467E-15	1.9289E-16	690.09
35	221537.5-173804	333.906395	-17.634663	914.24	41.78	7.2003E-03	3.4891E-04	2.6941E-15	1.8641E-16	679.80
36	221549.0-174626	333.954257	-17.773938	927.03	42.85	6.0084E-03	2.9098E-04	2.6140E-15	1.7198E-16	661.50
37	221623.1-174057	334.096539	-17.682732	1112.17	47.15	1.7668E-02	8.2171E-04	6.4995E-15	4.0342E-16	714.38
38	221507.0-173938	333.779452	-17.660686	921.15	42.98	7.0736E-03	3.4854E-04	4.5170E-15	2.3377E-16	609.90
39	221542.9-173959	333.929091	-17.666415	799.25	40.41	5.4619E-03	2.8769E-04	3.9411E-15	2.0854E-16	547.80
40	221547.5-174312	333.948254	-17.720030	937.00	43.78	5.7897E-03	2.7948E-04	2.9808E-15	1.7571E-16	546.80
41	221530.5-174617	333.877364	-17.771501	952.96	46.52	5.0532E-03	2.5173E-04	2.5063E-15	1.6069E-16	480.71
42	221448.6-174029	333.702677	-17.674919	830.10	40.65	8.5102E-03	4.5935E-04	4.1117E-15	2.6694E-16	533.46

Table 2: continued.

id	XMMU J	RA (J2000)	DEC (J2000)	CTS	CTS.ERR	RATE s <sup>-1</sup>	RATE.ERR s <sup>-1</sup>	FLUX erg s <sup>-1</sup> cm <sup>-2</sup>	FLUX.ERR erg s <sup>-1</sup> cm <sup>-2</sup>	LIKE
43	221549.1-173831	333.954899	-17.642010	841.95	41.49	7.7552E-03	4.0019E-04	3.9251E-15	2.4183E-16	500.98
44	221624.6-174132	334.102743	-17.692495	792.78	41.92	1.1991E-02	7.1817E-04	6.1366E-15	3.9355E-16	418.25
45	221525.5-175806	333.856547	-17.968610	437.76	26.32	4.4354E-03	2.8954E-04	1.3484E-14	9.6269E-16	438.31
46	221539.6-174904	333.915024	-17.817804	690.02	39.50	4.8411E-03	2.8226E-04	2.4834E-15	1.7659E-16	340.56
47	221510.3-174550	333.793183	-17.763913	718.95	42.68	5.0938E-03	3.3868E-04	2.9303E-15	1.9600E-16	382.03
48	221537.0-174939	333.904542	-17.827715	653.84	38.58	4.7292E-03	2.8683E-04	2.4667E-15	1.8086E-16	329.29
49	221533.2-173605	333.888472	-17.601558	418.09	34.72	3.6270E-03	3.2014E-04	2.1475E-15	2.1105E-16	120.43
50	221532.5-173617	333.885720	-17.604918	558.44	36.71	5.2015E-03	3.6571E-04	2.6491E-15	2.1842E-16	242.32
51	221607.0-175309	334.029369	-17.885877	711.95	39.15	9.3304E-03	5.7522E-04	4.9436E-15	3.2962E-16	375.44
52	221541.4-173755	333.922737	-17.632024	620.83	37.18	5.0871E-03	3.2448E-04	2.7357E-15	1.9574E-16	315.86
53	221537.2-173616	333.905012	-17.604670	583.90	36.64	5.4056E-03	3.6808E-04	2.6187E-15	2.1107E-16	273.42
54	221556.6-174709	333.986018	-17.785872	592.38	36.75	4.5939E-03	3.0124E-04	1.1928E-15	1.4101E-16	297.92
55	221606.2-174705	334.025953	-17.784883	577.22	38.09	7.0667E-03	5.0143E-04	4.0807E-15	3.0660E-16	305.91
56	221535.0-175020	333.896240	-17.839051	526.96	35.82	3.6081E-03	2.5471E-04	2.2061E-15	1.6417E-16	237.73
57	221531.3-173517	333.880784	-17.588330	509.70	33.62	4.8803E-03	3.5481E-04	3.0692E-15	2.2701E-16	252.17
58	221516.6-175041	333.819533	-17.844926	506.02	34.52	3.9869E-03	2.8475E-04	1.8671E-15	1.7185E-16	230.04
59	221526.1-174312	333.858853	-17.720205	486.41	37.12	2.5622E-03	2.0280E-04	1.5101E-15	1.3340E-16	175.48
60	221454.1-173547	333.725814	-17.596615	552.84	37.16	8.7027E-03	7.5140E-04	3.4430E-15	3.1728E-16	300.84
61	221543.2-175806	333.930041	-17.968480	401.57	29.39	6.2592E-03	6.2006E-04	8.7565E-15	7.7945E-16	248.63
62	221459.9-175202	333.749733	-17.867305	507.61	36.55	5.2413E-03	4.1488E-04	2.5523E-15	2.3283E-16	208.47
63	221510.7-173641	333.794985	-17.611389	449.13	33.57	4.4169E-03	3.5899E-04	2.1658E-15	2.0004E-16	193.35
64	221453.5-174946	333.723102	-17.829514	493.43	35.85	4.8469E-03	3.9453E-04	2.6456E-15	2.2460E-16	204.58
65	221529.8-174748	333.874290	-17.796738	462.64	35.45	2.6496E-03	2.0690E-04	1.0310E-15	1.1550E-16	179.60
66	221621.2-175109	334.088610	-17.852703	483.68	34.25	7.5763E-03	6.2482E-04	4.3488E-15	3.5215E-16	198.37
67	221603.4-173830	334.014555	-17.641942	456.91	35.08	5.4411E-03	4.8024E-04	2.7041E-15	2.5797E-16	161.33
68	221446.0-175126	333.691819	-17.857276	355.88	28.83	3.3810E-03	3.0942E-04	4.5092E-15	4.4296E-16	166.67
69	221504.5-174221	333.769133	-17.706066	345.07	34.36	2.8231E-03	3.2727E-04	1.9246E-15	1.8433E-16	137.84
70	221513.9-175437	333.808075	-17.910511	436.39	33.66	4.9176E-03	4.2355E-04	1.2396E-15	1.8154E-16	163.18
71	221510.6-173112	333.794304	-17.520005	318.72	25.67	4.1261E-03	3.5818E-04	6.7719E-15	6.0305E-16	171.22
72	221544.5-173908	333.935687	-17.652284	429.90	34.24	3.4895E-03	2.8924E-04	5.9804E-16	1.1922E-16	148.86
73	221542.9-175503	333.928928	-17.917555	408.78	33.29	4.3672E-03	3.9766E-04	2.6423E-15	2.3559E-16	147.53
74	221617.0-175139	334.070839	-17.861077	392.86	30.71	5.7572E-03	4.9632E-04	3.3951E-15	3.1041E-16	161.63
75	221538.4-174147	333.910385	-17.696620	419.10	42.22	3.2629E-03	5.6371E-04	1.8612E-15	1.9972E-16	139.72
76	221559.9-173839	333.999962	-17.644183	306.79	32.08	3.1403E-03	3.6153E-04	1.2858E-15	1.7803E-16	75.06
77	221440.3-174612	333.668018	-17.770002	321.60	27.80	2.9596E-03	2.8242E-04	4.1462E-15	4.2464E-16	134.03
78	221532.6-174245	333.886187	-17.712717	380.88	34.27	2.1821E-03	1.9970E-04	9.9128E-16	1.1796E-16	113.37
79	221441.4-174550	333.672792	-17.764051	304.33	27.38	2.7432E-03	2.7200E-04	3.6416E-15	3.9075E-16	117.72
80	221604.8-173408	334.020035	-17.569067	427.39	35.79	1.0617E-02	1.1034E-03	6.0691E-15	5.8293E-16	147.23
81	221558.3-175032	333.993130	-17.842495	373.38	32.00	3.4927E-03	3.2446E-04	2.0575E-15	1.9954E-16	121.45
82	221535.6-174650	333.898526	-17.780616	332.90	33.97	1.8412E-03	1.8906E-04	1.0270E-15	1.2417E-16	67.22
83	221502.1-173829	333.758836	-17.641588	377.43	32.86	3.5854E-03	3.3697E-04	1.4223E-15	1.7070E-16	115.23
84	221518.2-174607	333.825898	-17.768660	419.07	32.90	2.4087E-03	1.9137E-04	1.2273E-15	1.2154E-16	147.06
85	221601.2-174114	334.005235	-17.687340	326.18	31.26	2.9743E-03	3.0692E-04	1.6106E-15	1.7710E-16	105.88



Table 2: continued.

id	XMMU J	RA (J2000)	DEC (J2000)	CTS	CTS_ERR	RATE s <sup>-1</sup>	RATE_ERR s <sup>-1</sup>	FLUX erg s <sup>-1</sup> cm <sup>-2</sup>	FLUX_ERR erg s <sup>-1</sup> cm <sup>-2</sup>	LIKE
86	221509.1-173354	333.788301	-17.565166	386.88	34.04	4.6126E-03	4.5197E-04	2.4827E-15	2.5951E-16	105.71
87	221450.9-173528	333.712278	-17.591313	292.36	26.56	3.9818E-03	3.9202E-04	2.8865E-15	3.2268E-16	125.69
88	221551.4-174343	333.964212	-17.728762	331.82	32.10	2.1545E-03	2.1876E-04	1.0421E-15	1.2378E-16	86.50
89	221514.8-174054	333.812050	-17.681802	335.44	31.61	2.6101E-03	3.0139E-04	1.3727E-15	1.6102E-16	103.67
90	221545.7-175016	333.940707	-17.837830	315.07	29.43	2.3250E-03	2.3047E-04	1.3396E-15	1.4338E-16	119.47
91	221619.5-174940	334.081448	-17.827950	323.01	31.20	4.8379E-03	5.3511E-04	2.1064E-15	2.7095E-16	92.67
92	221530.7-175711	333.878292	-17.953200	247.16	26.32	2.5073E-03	3.0430E-04	3.8371E-15	4.3479E-16	85.58
93	221523.8-173138	333.849570	-17.527432	333.47	31.77	5.5750E-03	6.6631E-04	2.7492E-15	3.1642E-16	101.70
94	221605.0-174943	334.021065	-17.828753	284.28	32.27	3.3108E-03	4.3927E-04	1.1753E-15	1.8907E-16	66.71
95	221446.2-174652	333.692504	-17.781345	314.88	30.07	3.8338E-03	4.1950E-04	1.3377E-15	1.9531E-16	94.40
96	221557.5-174947	333.989903	-17.829865	295.17	30.80	2.4435E-03	2.7719E-04	1.7202E-15	1.8605E-16	73.45
97	221626.0-174813	334.108504	-17.803624	319.40	30.35	6.0750E-03	7.0784E-04	3.2370E-15	3.5466E-16	95.28
98	221612.7-173506	334.052933	-17.585167	233.53	30.37	3.7589E-03	5.6807E-04	1.5810E-15	2.8849E-16	36.91
99	221611.5-173454	334.047985	-17.581749	229.93	30.54	4.5200E-03	6.6173E-04	1.6761E-15	2.9855E-16	32.25
100	221514.2-173729	333.809446	-17.624759	359.15	32.81	3.1321E-03	3.0353E-04	1.4618E-15	1.6640E-16	94.60
101	221505.7-173545	333.773772	-17.595984	324.34	31.76	3.7101E-03	4.0517E-04	1.5697E-15	2.0528E-16	84.33
102	221600.4-174801	334.001707	-17.800485	299.22	28.93	2.5365E-03	2.5126E-04	1.4626E-15	1.6684E-16	86.46
103	221444.9-174619	333.687453	-17.772084	272.10	26.95	2.7571E-03	2.9729E-04	1.5569E-15	1.9343E-16	82.52
104	221533.8-175240	333.891171	-17.878005	277.42	38.21	3.6755E-03	7.5500E-04	8.0166E-16	1.8713E-16	44.22
105	221535.3-175252	333.897308	-17.881342	287.00	30.14	2.8695E-03	3.1855E-04	9.0303E-16	1.4654E-16	73.58
106	221456.5-175000	333.735755	-17.833461	313.58	32.37	3.1102E-03	3.5346E-04	6.0275E-16	1.3970E-16	69.27
107	221542.6-174604	333.927538	-17.767990	262.53	31.16	1.7321E-03	2.2438E-04	8.3767E-16	1.3330E-16	40.88
108	221543.2-174620	333.930074	-17.772380	180.16	27.89	1.3533E-03	2.3281E-04	4.8023E-16	1.1750E-16	31.28
109	221524.0-174633	333.850155	-17.776085	451.50	67.60	5.3394E-03	1.2114E-03	1.5680E-15	1.8481E-16	77.66
110	221507.8-175339	333.782835	-17.894286	279.08	30.33	2.9311E-03	3.5385E-04	1.5666E-15	1.9433E-16	70.11
111	221509.7-174626	333.790630	-17.774111	231.01	27.60	1.5329E-03	1.9186E-04	9.4029E-16	1.2800E-16	59.49
112	221558.5-175228	333.993921	-17.874547	229.81	28.43	2.5135E-03	3.6156E-04	1.4144E-15	1.9304E-16	47.61
113	221505.8-175008	333.774528	-17.835668	251.86	30.44	2.0241E-03	2.6596E-04	9.7108E-16	1.4650E-16	41.40
114	221504.5-175320	333.768953	-17.889022	269.70	29.69	2.9980E-03	3.9247E-04	1.6875E-15	2.1563E-16	57.14
115	221502.2-174851	333.759217	-17.814387	209.90	26.50	1.6398E-03	2.1715E-04	9.3159E-16	1.3442E-16	51.06
116	221635.9-174738	334.149762	-17.794135	204.27	23.59	4.7405E-03	6.3121E-04	3.9976E-15	5.0865E-16	74.70
117	221505.4-175513	333.772545	-17.920550	244.94	28.50	3.1263E-03	4.5731E-04	2.1881E-15	2.7249E-16	58.66
118	221530.2-174529	333.875968	-17.758159	228.59	29.87	1.1898E-03	1.5784E-04	7.1860E-16	1.0860E-16	33.59
119	221451.4-174750	333.714190	-17.797235	245.42	29.39	2.4219E-03	3.1716E-04	1.1572E-15	1.6752E-16	50.79
120	221500.2-174507	333.750989	-17.752100	240.42	29.78	1.8049E-03	2.4389E-04	9.7038E-16	1.3549E-16	48.16
121	221439.0-175010	333.662597	-17.836152	203.29	24.66	2.2605E-03	3.0626E-04	2.8638E-15	4.1697E-16	52.39
122	221452.8-173841	333.720121	-17.644845	276.46	31.61	3.5534E-03	5.2622E-04	1.6980E-15	2.4611E-16	62.23
123	221501.3-174626	333.755426	-17.773924	221.93	26.85	1.7066E-03	2.2217E-04	8.3636E-16	1.2784E-16	50.86
124	221623.3-173326	334.097375	-17.557294	156.70	18.53	4.6494E-03	5.6076E-04	4.1799E-15	6.3774E-16	64.24
125	221537.9-174421	333.908330	-17.739443	207.07	29.54	1.1061E-03	1.6030E-04	5.8825E-16	1.0765E-16	25.51
126	221543.5-175057	333.931403	-17.849439	221.04	29.47	1.8331E-03	2.5397E-04	7.3774E-16	1.3157E-16	29.36
127	221450.7-173812	333.711432	-17.636754	232.60	27.29	3.1957E-03	4.3751E-04	1.8318E-15	2.5519E-16	50.13
128	221546.5-174008	333.944153	-17.669057	214.25	27.69	1.4653E-03	1.9565E-04	6.2410E-16	1.2245E-16	36.89

Table 2: continued.

id	XMMU J	RA (J2000)	DEC (J2000)	CTS	CTS_ERR	RATE s <sup>-1</sup>	RATE_ERR s <sup>-1</sup>	FLUX erg s <sup>-1</sup> cm <sup>-2</sup>	FLUX_ERR erg s <sup>-1</sup> cm <sup>-2</sup>	LIKE
129	221617.9-173207	334.074904	-17.535412	161.90	20.34	3.2346E-03	4.1596E-04	3.0626E-15	4.6628E-16	54.57
130	221507.7-174046	333.782459	-17.679529	203.38	27.10	1.4330E-03	2.0712E-04	7.4339E-16	1.1719E-16	44.57
131	221508.8-175410	333.787074	-17.902934	196.35	28.96	2.1690E-03	3.6708E-04	7.2618E-16	1.6142E-16	30.65
132	221536.9-173527	333.903939	-17.590893	252.73	30.57	2.6688E-03	3.4929E-04	5.3624E-16	1.3985E-16	40.41
133	221532.9-175328	333.887278	-17.891194	225.03	28.46	2.2085E-03	3.1984E-04	1.0372E-15	1.6384E-16	41.27
134	221530.7-174434	333.878156	-17.742942	214.35	30.19	1.1296E-03	1.6067E-04	4.9376E-16	9.8869E-17	30.68
135	221545.9-174706	333.941616	-17.785202	112.24	23.29	7.2823E-04	1.7478E-04	6.5870E-16	1.3132E-16	10.10
136	221613.2-174505	334.055378	-17.751408	187.08	26.02	2.0612E-03	3.0888E-04	1.0859E-15	1.8099E-16	27.38
137	221515.7-173633	333.815657	-17.609358	218.21	28.03	1.9266E-03	2.8059E-04	7.8658E-16	1.4546E-16	44.37
138	221541.5-174419	333.923020	-17.738650	214.41	30.70	1.4439E-03	2.5404E-04	5.5775E-16	1.1914E-16	32.74
139	221605.0-174806	334.021155	-17.801713	193.51	26.78	1.9247E-03	2.8462E-04	1.1438E-15	1.7160E-16	31.55
140	221532.2-174001	333.884461	-17.666957	222.41	28.42	1.4799E-03	1.9661E-04	5.6068E-16	1.0000E-16	39.59
141	221529.6-174709	333.873712	-17.785899	163.78	27.83	9.1735E-04	1.5762E-04	4.4971E-16	9.5280E-17	18.05
142	221559.9-174146	333.999999	-17.696356	206.19	28.14	1.7072E-03	2.5432E-04	8.1035E-16	1.3815E-16	32.70
143	221504.9-174456	333.770550	-17.748994	192.02	26.16	1.3624E-03	1.8966E-04	8.1102E-17	6.6935E-17	35.19
144	221611.8-173858	334.049526	-17.649682	163.00	23.28	1.9798E-03	3.3258E-04	1.4243E-15	2.3275E-16	33.10
145	221513.6-174613	333.806783	-17.770532	213.51	29.43	1.3021E-03	1.8292E-04	6.4338E-16	1.0392E-16	29.57
146	221449.5-173920	333.706258	-17.655671	168.78	27.74	1.7417E-03	3.3656E-04	9.9768E-16	1.7848E-16	18.62
147	221450.7-175119	333.711632	-17.855499	180.01	24.23	1.8747E-03	2.6503E-04	1.2204E-15	2.8272E-16	38.66
148	221624.5-174938	334.102416	-17.827352	191.90	27.53	3.3783E-03	5.5077E-04	1.7489E-15	2.6860E-16	28.33
149	221539.0-173119	333.912544	-17.522026	167.33	24.53	3.3423E-03	5.4360E-04	1.6780E-15	2.8558E-16	30.44
150	221532.7-175509	333.886357	-17.919247	174.00	27.12	1.7268E-03	3.1127E-04	8.7398E-16	1.6985E-16	23.06
151	221605.7-175110	334.024020	-17.852792	167.81	27.40	1.9892E-03	3.7265E-04	8.3255E-16	1.7342E-16	18.37
152	221615.2-173627	334.063555	-17.607502	213.31	30.44	3.4878E-03	5.8804E-04	1.3153E-15	2.5271E-16	28.63
153	221501.8-174916	333.757866	-17.821314	139.17	25.34	1.0660E-03	2.0970E-04	6.3370E-16	1.3064E-16	13.15
154	221522.6-175253	333.844350	-17.881655	165.38	26.19	1.5431E-03	2.5745E-04	8.2095E-16	1.4262E-16	20.04
155	221540.8-175432	333.920229	-17.908905	183.07	26.46	1.9115E-03	2.9728E-04	1.0665E-15	1.7331E-16	25.08
156	221544.3-174145	333.934829	-17.695985	171.47	26.18	1.1352E-03	1.7987E-04	4.3198E-16	1.0467E-16	22.12
157	221608.2-174317	334.034406	-17.721614	163.99	25.56	1.6894E-03	2.8848E-04	6.3314E-16	1.4454E-16	31.07
158	221543.9-175326	333.933027	-17.890761	158.42	24.82	1.5230E-03	2.5551E-04	9.2605E-16	1.5377E-16	24.99
159	221541.6-174514	333.923698	-17.754074	152.42	26.08	9.7070E-04	2.1571E-04	7.2605E-16	1.3548E-16	17.92
160	221550.5-174105	333.960556	-17.684801	165.02	26.69	1.5666E-03	2.8532E-04	9.4450E-16	1.5638E-16	19.84
161	221604.4-175438	334.018733	-17.910626	152.43	22.32	1.6728E-03	2.7743E-04	2.3060E-15	3.9874E-16	32.12
162	221534.2-174208	333.892745	-17.702468	203.55	28.33	1.1037E-03	1.6301E-04	4.8351E-16	9.5412E-17	26.70
163	221603.1-173012	334.013267	-17.503352	102.89	16.61	2.0534E-03	3.4343E-04	1.5325E-15	3.7449E-16	29.16
164	221517.8-173133	333.824583	-17.525972	138.95	24.94	1.9345E-03	3.8428E-04	8.1841E-16	2.1629E-16	15.99
165	221544.0-173108	333.933701	-17.519064	159.33	25.73	2.8039E-03	5.3760E-04	1.8033E-15	3.1303E-16	23.70
166	221522.5-174816	333.843975	-17.804559	152.20	26.30	8.6028E-04	1.5545E-04	4.1050E-16	9.6968E-17	14.26
167	221612.0-175226	334.050376	-17.874015	140.02	23.04	2.4173E-03	4.7376E-04	1.6116E-15	2.7927E-16	23.23
168	221450.5-174931	333.710539	-17.825319	161.38	25.30	1.5687E-03	2.8186E-04	9.3479E-16	1.6360E-16	22.36
169	221602.8-173909	334.012011	-17.652545	119.04	25.70	1.2760E-03	3.0655E-04	2.5314E-16	1.2820E-16	7.51
170	221448.5-175112	333.702111	-17.853408	132.00	22.64	1.2297E-03	2.2957E-04	1.5324E-15	3.2933E-16	15.26
171	221509.8-175242	333.790909	-17.878568	171.71	25.90	1.8072E-03	2.9053E-04	4.4656E-16	1.1739E-16	20.87

Table 2: continued.

id	XMMU J	RA (J2000)	DEC (J2000)	CTS	CTS.ERR	RATE s <sup>-1</sup>	RATE.ERR s <sup>-1</sup>	FLUX erg s <sup>-1</sup> cm <sup>-2</sup>	FLUX.ERR erg s <sup>-1</sup> cm <sup>-2</sup>	LIKE
172	221545.4-174451	333.939532	-17.747571	134.18	26.48	8.6005E-04	1.7140E-04	9.0139E-17	6.7192E-17	9.01
173	221547.0-174614	333.946108	-17.770613	148.34	26.77	9.0076E-04	1.7351E-04	8.7558E-17	6.9359E-17	15.27
174	221555.5-174648	333.981514	-17.780248	138.18	26.04	1.1653E-03	2.1837E-04	1.1766E-16	7.7644E-17	9.28
175	221458.1-175349	333.742087	-17.897092	163.84	24.39	2.3743E-03	3.8987E-04	8.4123E-16	1.9440E-16	22.78
176	221559.1-174413	333.996454	-17.737162	141.87	24.16	1.2638E-03	2.1851E-04	3.9326E-16	1.1100E-16	18.40
177	221537.1-175432	333.904736	-17.908937	132.74	23.34	1.3037E-03	3.4061E-04	7.1496E-16	1.7286E-16	16.41
178	221507.5-173728	333.781510	-17.624572	146.81	25.35	1.3837E-03	2.6653E-04	6.1586E-16	1.3279E-16	18.38
179	221540.7-173954	333.919948	-17.665055	136.44	25.86	9.8477E-04	1.9427E-04	5.2304E-16	1.1342E-16	12.42
180	221616.9-175045	334.070530	-17.846057	142.02	24.35	1.8876E-03	3.7265E-04	1.1610E-15	2.1787E-16	16.08
181	221504.4-174527	333.768389	-17.757558	171.89	30.11	2.1357E-03	5.0847E-04	8.5266E-16	1.7844E-16	19.12
182	221515.2-173321	333.813446	-17.555838	110.51	23.73	1.3603E-03	3.3318E-04	6.8083E-16	1.8313E-16	6.38
183	221453.9-174127	333.724610	-17.691056	145.34	24.41	1.4038E-03	2.6043E-04	8.1552E-16	1.5271E-16	20.02
184	221607.3-175045	334.030770	-17.845945	127.36	24.43	1.6730E-03	3.5708E-04	1.4456E-16	1.1924E-16	12.63
185	221526.5-173016	333.860758	-17.504584	105.80	21.04	1.9186E-03	4.3486E-04	3.2869E-16	1.4431E-16	34.14
186	221551.2-174909	333.963544	-17.819426	138.80	25.65	1.0305E-03	2.0841E-04	2.4993E-16	9.9389E-17	13.44
187	221538.9-173955	333.912450	-17.665432	124.12	24.19	8.6604E-04	1.7670E-04	2.1539E-16	8.0700E-17	10.39
188	221527.3-172947	333.864009	-17.496464	188.75	24.50	1.1715E-02	1.6528E-03	7.6535E-15	1.4070E-15	56.06
189	221628.5-174037	334.119073	-17.677008	157.05	25.05	2.7480E-03	4.9763E-04	1.7914E-15	2.8634E-16	22.70
190	221504.4-175644	333.768391	-17.945715	104.83	19.71	1.9445E-03	4.0452E-04	1.1880E-15	3.5916E-16	17.77
191	221508.6-174202	333.786175	-17.700588	156.06	25.67	9.9608E-04	1.7595E-04	2.9458E-16	7.8627E-17	22.10
192	221607.1-173603	334.029850	-17.600985	129.90	24.14	2.0073E-03	4.3831E-04	6.7093E-16	2.0272E-16	15.62
193	221600.5-173407	334.002414	-17.568625	143.36	25.25	2.4112E-03	4.7822E-04	4.6564E-16	1.6977E-16	13.20
194	221447.4-174801	333.697703	-17.800540	159.17	26.51	1.8924E-03	3.5230E-04	6.4570E-16	1.5986E-16	16.00
195	221515.6-173755	333.815402	-17.632222	149.50	26.24	1.3568E-03	2.4244E-04	1.2441E-16	8.3838E-17	11.73
196	221531.8-174931	333.882571	-17.825333	143.73	25.07	9.2705E-04	1.7243E-04	4.4520E-16	9.7470E-17	14.36
197	221603.1-175351	334.013324	-17.897506	111.67	22.90	1.3876E-03	3.3649E-04	6.6689E-16	1.9034E-16	12.25
198	221602.7-175312	334.011648	-17.886689	157.57	27.47	1.9770E-03	4.0769E-04	6.0970E-16	1.7252E-16	13.60
199	221457.8-175433	333.740985	-17.909421	76.19	16.51	7.9713E-04	1.9302E-04	1.5743E-15	4.5230E-16	12.12
200	221553.7-173219	333.973997	-17.538760	157.07	26.76	3.0129E-03	5.9347E-04	1.1634E-15	2.6329E-16	15.41
201	221511.9-173908	333.799733	-17.652383	103.46	22.10	8.2547E-04	2.1154E-04	2.9860E-16	9.7667E-17	12.93
202	221539.3-172926	333.914113	-17.490632	110.27	21.17	4.0991E-03	8.8204E-04	2.2648E-15	6.1837E-16	16.81
203	221606.5-174340	334.027320	-17.727824	127.63	26.07	1.1647E-03	2.7049E-04	4.9838E-16	1.3462E-16	12.39
204	221557.5-175637	333.989802	-17.943826	112.67	21.87	1.4385E-03	3.2274E-04	1.5499E-15	3.7886E-16	12.12
205	221505.2-175444	333.771707	-17.912317	106.68	25.24	1.2428E-03	3.7959E-04	5.9543E-16	1.5859E-16	6.34
206	221558.0-173700	333.991725	-17.616938	114.30	23.82	1.3841E-03	3.1384E-04	7.1985E-17	9.0811E-17	8.04
207	221443.1-174544	333.679981	-17.762393	122.87	31.50	2.1788E-03	1.1763E-03	7.0389E-16	2.0631E-16	11.32
208	221513.8-174717	333.807732	-17.788199	128.24	25.57	7.6916E-04	1.6347E-04	4.4839E-16	9.9153E-17	10.06
209	221503.7-173911	333.765681	-17.653303	113.01	23.32	8.5155E-04	1.8975E-04	3.6444E-16	1.1368E-16	8.43
210	221606.7-174305	334.028325	-17.718231	104.75	23.09	8.5331E-04	2.1204E-04	5.6141E-16	1.4690E-16	6.65
211	221506.1-174515	333.775430	-17.754226	106.99	25.56	8.4430E-04	3.0472E-04	5.8006E-16	1.3739E-16	10.11
212	221543.2-174355	333.930048	-17.732016	105.82	22.23	6.2379E-04	1.3293E-04	1.5039E-16	6.2665E-17	9.47
213	221443.9-174502	333.683075	-17.750592	109.27	22.25	1.1498E-03	2.6274E-04	6.4993E-16	1.4694E-16	11.46
214	221438.2-174858	333.659367	-17.816144	110.56	21.49	1.3015E-03	2.8306E-04	1.2886E-15	3.3305E-16	12.27

Table 2: continued.

id	XMMU J	RA (J2000)	DEC (J2000)	CTS	CTS_ERR	RATE s <sup>-1</sup>	RATE_ERR s <sup>-1</sup>	FLUX erg s <sup>-1</sup> cm <sup>-2</sup>	FLUX_ERR erg s <sup>-1</sup> cm <sup>-2</sup>	LIKE
215	221508.4-174808	333.785169	-17.802326	129.64	24.18	9.0988E-04	1.8083E-04	3.5421E-17	5.6016E-17	11.67
216	221628.1-174851	334.117191	-17.814424	149.29	30.38	6.3251E-03	1.3912E-03	3.3354E-15	7.9132E-16	14.73
217	221521.2-174059	333.838635	-17.683205	136.85	25.56	8.5531E-04	1.6306E-04	2.8556E-16	8.5341E-17	11.00
218	221537.4-175544	333.906186	-17.929076	127.38	26.78	2.4576E-03	6.6602E-04	5.6012E-16	1.9479E-16	8.22
219	221614.0-173457	334.058391	-17.582515	147.56	26.76	2.7046E-03	5.4685E-04	6.8730E-16	2.1542E-16	9.79
220	221520.3-175309	333.834620	-17.885846	119.68	23.42	1.1053E-03	2.3277E-04	5.1009E-16	1.2978E-16	10.16
221	221501.8-173932	333.757674	-17.658957	103.77	22.93	8.5580E-04	2.2138E-04	2.3308E-16	9.7395E-17	7.28
222	221519.9-175635	333.833213	-17.943285	94.25	24.37	1.5904E-03	6.1403E-04	8.1257E-16	2.2771E-16	6.09
223	221457.6-173416	333.740344	-17.571356	122.58	24.61	1.5971E-03	3.7688E-04	7.4536E-16	2.0375E-16	10.51
224	221437.8-174642	333.657774	-17.778376	69.53	17.62	6.6640E-04	1.9802E-04	1.2724E-15	3.1036E-16	9.50
225	221606.8-175544	334.028374	-17.929067	62.59	18.95	9.0571E-04	9.0286E-04	1.5260E-15	5.0487E-16	7.72
226	221533.1-173148	333.887945	-17.530198	144.48	26.64	2.2290E-03	4.8357E-04	6.9333E-16	1.9586E-16	13.76
227	221541.3-173619	333.922374	-17.605471	112.55	23.71	9.9635E-04	2.4904E-04	3.7913E-16	1.2188E-16	9.15
228	221548.2-173958	333.950885	-17.666296	117.51	24.76	1.1286E-03	2.4414E-04	3.4064E-16	1.1171E-16	7.92
229	221524.8-174226	333.853395	-17.707326	110.74	24.83	5.4354E-04	1.3390E-04	8.3314E-17	6.1275E-17	6.29
230	221612.3-175114	334.051344	-17.854086	111.07	22.90	1.7305E-03	4.5601E-04	9.4355E-16	2.3026E-16	7.47
231	221523.9-175445	333.849678	-17.912587	105.55	22.30	1.0253E-03	2.5211E-04	5.2468E-16	1.3723E-16	8.91
232	221520.9-174614	333.837220	-17.770620	122.92	25.65	6.4579E-04	1.4333E-04	2.1947E-16	7.7028E-17	7.34
233	221616.5-173704	334.069149	-17.617824	112.47	24.47	1.9302E-03	4.3882E-04	5.6538E-16	1.9366E-16	6.65
234	221525.5-175037	333.856348	-17.843654	110.65	23.83	8.9668E-04	2.2337E-04	4.5063E-16	1.1510E-16	9.20
235	221544.6-173945	333.936222	-17.662649	128.43	25.77	1.0541E-03	2.0679E-04	3.1837E-16	9.6549E-17	8.92
236	221618.1-174856	334.075641	-17.815738	98.42	22.73	1.4224E-03	3.8210E-04	7.1815E-16	1.8719E-16	6.54
237	221447.7-174714	333.699110	-17.787251	84.43	21.76	1.2002E-03	3.1342E-04	2.6863E-16	1.2282E-16	7.28
238	221452.6-173914	333.719543	-17.653977	91.61	22.75	1.0820E-03	4.9257E-04	1.0428E-16	1.1991E-16	9.40
239	221638.4-174339	334.160377	-17.727624	59.81	17.65	1.2844E-03	4.6764E-04	1.2028E-15	3.8676E-16	7.60
240	221614.6-173539	334.061037	-17.594261	133.17	27.23	2.7801E-03	6.0715E-04	3.1664E-16	1.8921E-16	7.08
241	221442.0-174406	333.675002	-17.735251	94.63	22.36	1.0129E-03	2.9243E-04	7.4966E-16	1.6894E-16	6.76
242	221524.6-173725	333.852530	-17.623782	103.86	23.97	7.6511E-04	2.0485E-04	4.4214E-16	1.1536E-16	6.29
243	221439.8-173826	333.665983	-17.640695	120.84	25.93	1.4971E-03	4.3830E-04	8.9755E-16	2.1062E-16	9.30
244	221501.0-174119	333.754236	-17.688697	114.09	23.81	9.3127E-04	2.1229E-04	2.5781E-16	8.8504E-17	8.51
245	221619.0-173302	334.079361	-17.550831	47.15	14.10	9.7055E-04	3.3741E-04	4.1663E-16	2.6775E-16	6.83
246	221516.0-174554	333.816919	-17.765059	78.96	20.27	6.0219E-04	1.4849E-04	1.6857E-17	4.8502E-17	6.11

Table 5: Complete list of all spectra that have enough S/N, sorted according to the brightness in the  $z'$  passband. The  $z$  flag is defined as follows: (0) good (1) trustworthy (2) tentative. The template column indicates which template has been used to identify the object or determine its redshift. All stars listed are late types, primarily of the K and M classes. The ID is indicated for cluster members as they appear in Figures 7,13,16,19,22 and in Table 6. The  $z'$  and  $H$  brightness are listed as AUTO magnitudes. The magnitude flag is (0) when good and (1) when possibly affected by photometric effects.

#	ID	$\alpha$ (J2000)	$\delta$ (J2000)	$z$	$\delta z$	$z$ flag	template	$z'$ (mag)	$H$ (mag)	mag flag
1		22:15:06.2	-17:53:00.3	0	—	0	star	15.72	15.16	1
2		22:15:47.5	-17:39:20.7	0	—	1	star	17.33	17.28	1
3		22:15:31.0	-17:42:44.0	0	—	0	star	17.40	16.92	0
4	ext#3 B	22:15:01.4	-17:50:35.9	0.3365	0.0001	0	passive	17.48	16.65	0
5	ext#5 K	22:16:05.1	-17:49:42.5	1.2231	< 0.0001	0	qso	17.66	17.56	0
6	ext#6 A	22:15:03.6	-17:52:10.1	0.4080	< 0.0001	0	passive	17.69	16.80	0
7		22:16:06.5	-17:50:01.8	0.4597	0.0016	2	passive	17.77	18.02	0
8		22:15:50.6	-17:43:54.0	0	—	0	star	17.89	17.46	0
9		22:15:06.8	-17:48:59.9	0	—	0	star	18.02	17.42	0
10		22:15:40.1	-17:48:44.6	0	—	0	star	18.09	17.36	0
11		22:15:37.7	-17:43:43.4	0	—	0	star	18.32	17.74	0
12		22:14:50.3	-17:50:00.0	0.2662	< 0.0001	0	emission	18.37	17.82	0
13		22:14:58.3	-17:54:33.6	0	—	0	star	18.43	17.95	0
14	ext#1 A	22:15:36.7	-17:45:32.9	0.4069	0.0001	0	passive	18.45	17.59	0
15	ext#3 F	22:14:59.2	-17:50:18.9	0.3372	< 0.0001	1	emission	18.56	17.82	0
16		22:15:00.8	-17:49:51.5	0.2320	< 0.0001	0	emission	18.66	18.02	0
17	ext#3 M	22:15:02.1	-17:52:47.0	0.3389	0.0001	0	passive	18.66	17.90	0
18	ext#3 D	22:15:01.0	-17:50:24.2	0.3351	0.0001	0	passive	18.79	17.98	0
19	ext#3 N	22:15:02.4	-17:52:56.9	0.3378	0.0001	0	passive	18.81	17.76	0
20		22:14:59.2	-17:50:25.2	0.2320	< 0.0001	0	emission	19.00	18.53	0
21		22:14:49.6	-17:49:36.8	0	—	0	star	19.14	18.48	0
22		22:16:14.2	-17:40:00.4	0	—	0	star	19.23	18.61	0
23		22:15:41.4	-17:49:24.1	0	—	0	star	19.24	18.75	0
24		22:14:51.3	-17:49:00.6	0.2886	< 0.0001	0	passive	19.26	24.55	0
25		22:15:01.8	-17:51:55.8	0.2464	< 0.0001	0	emission	19.30	18.26	0
26	ext#1 C	22:15:37.1	-17:45:20.4	0.4094	0.0001	0	passive	19.33	18.44	0
27		22:15:01.9	-17:49:14.6	0.5684	0.0001	0	passive	19.35	18.84	0
28	ext#1 B	22:15:36.8	-17:45:43.2	0.4113	0.0001	0	passive	19.35	18.58	0
29		22:15:42.8	-17:48:14.6	0.2457	< 0.0001	0	emission	19.35	18.74	0
30		22:16:06.8	-17:50:01.5	0.4578	0.0002	2	passive	19.39	18.61	0
31		22:15:02.7	-17:48:10.8	0.2274	< 0.0001	1	emission	19.40	21.56	0
32		22:15:01.1	-17:50:16.8	0.6121	0.0001	0	emission	19.41	18.67	1
33		22:15:39.2	-17:48:31.6	0	—	0	star	19.42	18.99	0
34	ext#3 Q	22:15:33.5	-17:45:43.2	0.3358	0.0001	0	passive	19.44	18.40	0
35	ext#3 J	22:14:55.4	-17:49:41.0	0.3367	0.0001	0	passive	19.45	18.72	0
36		22:16:14.1	-17:38:45.2	0.3721	< 0.0001	0	passive	19.53	18.80	0
37		22:15:12.4	-17:52:57.9	0	—	0	star	19.54	19.50	0
38		22:15:40.2	-17:44:36.4	0.3714	< 0.0001	0	emission	19.55	18.39	0
39		22:14:49.3	-17:49:50.4	0.2746	< 0.0001	0	emission	19.59	19.38	0
40	ext#6 H	22:15:01.4	-17:53:53.7	0.4194	< 0.0001	0	emission	19.67	18.83	0
41	ext#6 M	22:15:01.4	-17:49:19.8	0.4095	< 0.0001	0	passive	19.71	19.90	0
42	ext#1 F	22:15:33.0	-17:46:41.2	0.4065	0.0001	0	passive	19.71	18.89	0
43	ext#6 I	22:14:59.6	-17:53:56.8	0.4103	< 0.0001	0	emission	19.74	18.85	0
44		22:14:49.4	-17:49:43.6	0.2990	< 0.0001	0	emission	19.74	19.45	0
45		22:15:44.5	-17:49:15.4	0.4435	0.0002	2	passive	19.76	18.99	0
46		22:15:03.6	-17:51:07.2	0.4384	< 0.0001	0	emission	19.80	19.00	0
47		22:16:02.9	-17:41:26.2	0	—	0	star	19.80	18.95	1
48		22:15:27.5	-17:47:49.4	0	—	0	star	19.82	19.27	0
49	ext#3 L	22:15:07.3	-17:51:27.6	0.3391	0.0001	0	passive	19.83	19.08	0
50	ext#6 J	22:14:59.2	-17:49:58.8	0.4035	< 0.0001	1	emission	19.84	19.45	1
51	ext#6 D	22:15:05.2	-17:52:42.5	0.4080	< 0.0001	1	emission	19.88	19.19	0
52		22:16:02.3	-17:39:49.6	1.4588	< 0.0001	1	qso	19.88	19.38	0
53		22:15:43.8	-17:45:04.0	0.3699	0.0001	0	passive	19.89	19.07	0
54	ext#1 K	22:15:36.3	-17:42:26.4	0.4022	0.0001	0	passive	19.96	19.17	0
55	ext#1 G	22:15:35.9	-17:43:59.6	0.4098	0.0002	0	passive	19.96	18.95	1

Table 5: continued.

#	ID	$\alpha$ (J2000)	$\delta$ (J2000)	$z$	$\delta z$	$z$ flag	template	$z'$ (mag)	$H$ (mag)	mag flag
56		22:16:03.7	-17:51:40.6	0.3330	< 0.0001	0	passive	19.97	19.57	0
57		22:15:32.1	-17:46:29.6	0.4300	< 0.0001	1	emission	20.01	19.16	0
58		22:15:59.4	-17:41:33.7	0	—	0	star	20.02	19.42	1
59	ext#1 H	22:15:38.7	-17:43:58.1	0.4057	0.0001	1	passive	20.03	19.10	0
60	ext#3 P	22:15:33.4	-17:45:54.6	0.3372	< 0.0001	0	emission	20.03	19.41	0
61		22:15:34.3	-17:46:26.7	0.4515	< 0.0001	1	emission	20.09	19.41	0
62		22:15:58.5	-17:41:29.7	1.5158	0.0001	1	emission	20.12	19.97	1
63	ext#3 H	22:14:59.8	-17:49:38.7	0.3378	< 0.0001	0	emission	20.15	20.11	0
64	ext#1 J	22:15:38.4	-17:47:48.7	0.4091	0.0001	0	passive	20.18	19.40	0
65	ext#6 B	22:15:04.6	-17:52:04.5	0.4054	0.0001	0	passive	20.21	19.21	0
66		22:15:53.3	-17:41:51.2	0.9244	< 0.0001	1	passive	20.23	19.30	0
67		22:15:38.5	-17:47:32.6	0.6574	0.0001	0	emission	20.23	19.65	0
68		22:14:59.7	-17:53:52.9	0	—	0	star	20.23	20.19	0
69		22:15:03.2	-17:52:58.8	0.6655	< 0.0001	1	emission	20.26	19.36	0
70		22:15:38.8	-17:44:21.9	0.1297	< 0.0001	0	emission	20.27	20.01	0
71		22:15:00.8	-17:51:09.3	0.6119	< 0.0001	0	emission	20.28	19.69	0
72	ext#6 G	22:15:05.1	-17:53:46.4	0.4088	< 0.0001	0	emission	20.29	19.33	0
73		22:15:34.0	-17:47:12.5	0.4415	< 0.0001	0	emission	20.31	19.97	0
74		22:15:41.8	-17:45:13.0	0.4301	< 0.0001	0	emission	20.34	19.52	0
75	ext#3 E	22:15:02.0	-17:50:48.8	0.3391	0.0001	0	passive	20.39	19.67	0
76		22:15:01.7	-17:51:36.9	0.3120	< 0.0001	0	emission	20.41	21.78	1
77		22:15:52.2	-17:42:43.9	0	—	0	star	20.45	19.83	0
78		22:15:02.6	-17:47:44.1	0.2282	< 0.0001	2	emission	20.46	99.00	0
79	ext#3 G	22:15:01.1	-17:50:01.9	0.3350	0.0001	0	passive	20.48	19.65	0
80		22:15:43.8	-17:49:46.6	0.3329	< 0.0001	2	passive	20.49	20.77	0
81		22:15:51.4	-17:49:08.4	0.7205	0.0001	0	passive	20.53	19.49	0
82	ext#3 O	22:15:08.5	-17:53:16.0	0.3441	< 0.0001	1	emission	20.54	19.97	0
83	ext#6 E	22:15:04.0	-17:52:59.9	0.4132	< 0.0001	0	emission	20.55	20.09	0
84		22:16:01.1	-17:39:35.3	4.2099	0.0001	0	qso	20.60	20.28	0
85	ext#1 E	22:15:42.6	-17:45:24.9	0.4063	0.0001	0	passive	20.60	19.79	0
86	ext#6 N	22:14:54.3	-17:54:32.3	0.4180	< 0.0001	1	emission	20.62	20.03	1
87		22:15:07.8	-17:51:53.6	0.4407	< 0.0001	0	emission	20.62	20.17	0
88		22:14:47.9	-17:49:02.6	0.2768	< 0.0001	0	emission	20.63	99.00	0
89		22:15:32.0	-17:46:51.7	0.1925	< 0.0001	0	emission	20.63	19.97	0
90		22:15:02.1	-17:53:25.4	0.7951	0.0002	2	emission	20.65	20.04	0
91		22:15:52.7	-17:41:27.1	0.3719	< 0.0001	0	emission	20.65	20.16	0
92		22:15:48.4	-17:40:44.9	0	—	0	star	20.67	20.12	0
93		22:16:01.3	-17:52:28.3	0.5879	< 0.0001	0	passive	20.67	19.81	0
94		22:14:54.0	-17:50:32.7	0.4422	< 0.0001	0	emission	20.70	19.90	0
95	ext#1 D	22:15:39.3	-17:44:44.6	0.4081	< 0.0001	0	emission	20.71	20.21	0
96	ext#1 I	22:15:42.2	-17:43:42.6	0.4075	0.0001	1	passive	20.73	20.00	0
97	ext#6 L	22:15:15.5	-17:53:09.4	0.4068	0.0002	1	passive	20.78	19.99	0
98	ext#3 I	22:14:56.0	-17:51:25.0	0.3431	< 0.0001	0	passive	20.79	19.76	0
99	ext#3 K	22:14:55.2	-17:49:38.5	0.3406	0.0001	2	passive	20.80	20.11	0
100		22:16:04.4	-17:48:58.0	0.6262	0.0001	0	passive	20.81	19.75	0
101		22:15:04.8	-17:54:27.5	0	—	0	star	20.82	21.13	1
102		22:15:58.2	-17:51:45.6	0.9152	< 0.0001	0	emission	20.84	19.68	0
103		22:16:14.9	-17:38:49.5	0.7530	0.0001	0	emission	20.85	19.79	0
104		22:16:04.5	-17:39:08.8	0.7537	0.0001	0	passive	20.85	19.46	0
105		22:15:04.0	-17:51:41.1	0.2122	< 0.0001	0	emission	20.87	20.01	0
106		22:14:55.4	-17:55:05.4	0.7401	0.0002	0	emission	20.87	20.25	0
107		22:15:50.5	-17:41:18.3	0	—	0	star	20.88	20.51	0
108		22:16:00.2	-17:50:20.5	0	—	0	star	20.89	20.23	0
109	ext#4 D	22:15:56.8	-17:40:30.8	1.0045	0.0001	0	passive	20.93	19.64	0
110		22:15:44.3	-17:42:58.2	0.3531	< 0.0001	0	emission	20.93	20.71	0
111		22:15:54.4	-17:51:40.6	0	—	0	star	20.95	20.38	0
112		22:14:54.1	-17:52:40.7	0.4072	< 0.0001	0	emission	20.95	20.13	0
113		22:16:03.1	-17:50:50.4	0.9938	0.0001	0	passive	20.96	19.63	0
114		22:15:00.2	-17:53:32.9	0.5407	0.0001	0	emission	20.96	20.62	0
115		22:15:51.0	-17:40:10.3	0.0940	< 0.0001	0	emission	20.96	20.56	0



Table 5: continued.

#	ID	$\alpha$ (J2000)	$\delta$ (J2000)	$z$	$\delta z$	$z$ flag	template	$z'$ (mag)	$H$ (mag)	mag flag
116		22:15:52.5	-17:38:42.2	0	—	0	star	21.00	20.53	0
117		22:15:10.3	-17:53:20.0	0	—	0	star	21.01	20.77	0
118		22:14:56.1	-17:50:01.5	0.4426	< 0.0001	0	emission	21.02	20.71	0
119		22:15:49.1	-17:38:27.2	0.9127	0.0001	0	emission	21.04	20.44	0
120		22:14:58.4	-17:52:50.3	0.2602	< 0.0001	2	emission	21.09	20.66	0
121	ext#4 C	22:15:57.2	-17:40:26.6	1.0007	0.0003	0	passive	21.10	19.98	0
122		22:16:07.7	-17:39:12.9	0.8806	0.0002	0	passive	21.11	19.90	0
123		22:16:03.0	-17:39:16.4	0	—	0	star	21.12	19.73	0
124		22:15:00.3	-17:48:36.4	0.1954	< 0.0001	0	emission	21.14	99.00	0
125		22:15:52.5	-17:41:27.9	0	—	0	star	21.16	20.63	0
126		22:16:10.9	-17:51:08.5	0.6791	< 0.0001	0	emission	21.21	20.45	0
127	ext#4 B	22:15:57.5	-17:40:27.9	0.9962	0.0001	0	passive	21.22	19.87	0
128		22:15:59.0	-17:41:30.0	0	—	0	star	21.23	20.68	1
129	ext#4 A	22:15:57.4	-17:40:28.0	0.9985	0.0001	0	passive	21.24	19.87	0
130		22:15:59.9	-17:49:54.1	1.0674	0.0002	1	passive	21.24	20.32	0
131		22:16:05.8	-17:39:51.3	0.7825	0.0001	0	passive	21.28	20.32	0
132		22:16:04.1	-17:40:58.7	0.5732	0.0001	0	passive	21.28	20.11	1
133		22:15:54.9	-17:39:59.5	0	—	0	star	21.33	20.70	0
134		22:15:38.8	-17:47:43.4	0.3645	< 0.0001	1	emission	21.34	21.26	0
135		22:16:05.0	-17:40:27.6	0.2288	0.0004	1	passive	21.34	20.85	0
136	ext#4 J	22:16:00.0	-17:41:57.5	0.9991	0.0001	0	passive	21.35	19.99	1
137		22:15:57.6	-17:49:47.7	0.7354	0.0001	0	passive	21.37	20.44	0
138	ext#4 H	22:16:01.9	-17:40:00.7	0.9997	0.0001	0	passive	21.37	20.24	0
139		22:15:36.4	-17:43:09.6	0.1632	< 0.0001	2	emission	21.38	21.19	0
140		22:15:43.3	-17:50:34.6	0.7514	0.0001	0	passive	21.39	19.99	0
141		22:15:52.1	-17:52:29.1	1.0658	0.0001	0	passive	21.40	20.30	0
142		22:15:09.9	-17:54:08.7	0.6439	0.0003	0	passive	21.41	20.50	0
143		22:16:06.1	-17:51:10.2	0.8586	0.0001	0	emission	21.41	20.71	1
144		22:15:13.5	-17:53:12.3	0.4408	< 0.0001	0	emission	21.42	21.16	0
145		22:14:48.9	-17:49:40.4	0.2776	< 0.0001	1	emission	21.43	21.31	0
146		22:15:48.3	-17:41:08.4	0.7160	0.0001	0	emission	21.45	20.65	0
147		22:15:53.0	-17:50:37.4	0.6801	0.0001	0	passive	21.47	20.74	0
148	ext#4 I	22:16:00.7	-17:39:34.5	1.0010	0.0001	0	passive	21.48	20.05	0
149	ext#3 A	22:15:01.3	-17:50:44.8	0.3371	< 0.0001	1	emission	21.48	21.37	0
150		22:16:13.1	-17:38:55.6	0.8602	0.8500	0	passive	21.50	20.70	0
151		22:15:58.3	-17:51:45.4	0.9901	0.0001	0	emission	21.61	20.61	0
152		22:16:10.0	-17:51:03.4	1.0711	0.0001	0	emission	21.66	20.71	0
153		22:15:57.9	-17:40:20.4	1.4614	0.0002	2	passive	21.67	19.48	0
154		22:16:03.3	-17:47:31.3	0	—	0	star	21.69	21.07	0
155	ext#4 E	22:15:55.6	-17:40:51.7	0.9924	0.0001	0	passive	21.71	20.46	0
156		22:15:49.7	-17:40:26.6	0	—	0	star	21.71	21.06	0
157	ext#6 C	22:15:03.7	-17:52:33.6	0.4080	< 0.0001	2	emission	21.72	21.38	0
158		22:15:58.9	-17:52:19.8	0.7010	0.0001	0	passive	21.73	20.67	0
159		22:15:48.8	-17:40:04.8	1.2997	0.0001	1	passive	21.76	20.27	0
160	ext#5 C	22:15:56.3	-17:51:38.9	1.2219	0.0001	1	emission	21.81	20.28	0
161		22:16:05.0	-17:47:00.4	0	—	0	star	21.81	21.29	0
162		22:16:03.6	-17:38:29.6	1.4616	0.0003	0	qso	21.81	21.10	0
163		22:16:08.6	-17:39:24.2	0.8692	< 0.0001	0	emission	21.82	21.02	0
164		22:15:47.6	-17:49:55.0	0.7987	0.0001	0	passive	21.82	20.98	1
165		22:15:52.4	-17:52:14.2	1.3027	< 0.0001	0	qso	21.83	20.89	0
166		22:16:09.2	-17:52:14.8	0.3879	0.0001	2	passive	21.84	21.42	0
167	ext#5 H	22:15:57.7	-17:51:21.7	1.2219	0.0004	1	emission	21.85	21.26	0
168	ext#5 G	22:15:54.9	-17:51:56.5	1.2291	0.0001	0	passive	21.85	20.17	0
169	ext#4 G	22:15:53.6	-17:40:04.5	1.0029	0.0002	0	passive	21.86	20.35	1
170		22:15:50.5	-17:40:35.3	0.6326	0.0001	0	emission	21.87	21.22	0
171		22:16:09.5	-17:40:24.0	0	—	0	star	21.88	21.43	0
172		22:16:06.6	-17:50:33.7	0.9453	< 0.0001	0	emission	21.91	21.12	0
173		22:16:01.2	-17:38:56.1	0	—	0	star	21.95	20.97	0
174	ext#5 B	22:15:56.6	-17:51:36.0	1.2195	0.0006	0	emission	21.97	21.02	0
175		22:16:06.5	-17:39:22.7	1.0726	0.0001	0	emission	21.98	20.97	0

Table 5: continued.

#	ID	$\alpha$ (J2000)	$\delta$ (J2000)	$z$	$\delta z$	$z$ flag	template	$z'$ (mag)	$H$ (mag)	mag flag
176		22:16:02.5	-17:51:20.0	0.9992	0.0001	0	passive	21.99	20.68	0
177		22:16:13.6	-17:38:57.2	0.5203	0.0005	1	passive	22.08	21.13	0
178		22:15:48.8	-17:52:15.6	0	—	0	star	22.09	21.28	0
179		22:15:50.8	-17:51:02.2	0.8482	0.0001	0	emission	22.10	20.96	0
180		22:16:02.6	-17:47:07.2	0	—	0	star	22.11	21.67	0
181		22:16:10.8	-17:40:00.4	1.0481	0.0001	0	passive	22.13	20.80	0
182	ext#4 L	22:16:05.3	-17:39:58.8	0.9986	0.0001	0	passive	22.13	20.98	0
183	ext#5 A	22:15:56.5	-17:51:38.8	1.2374	0.0003	0	emission	22.14	21.46	0
184		22:16:13.1	-17:42:06.9	0.8680	0.0001	0	passive	22.14	21.09	0
185		22:16:02.0	-17:52:17.8	0.7093	0.0001	0	passive	22.15	20.78	0
186		22:15:45.3	-17:48:28.4	0.9143	0.0001	0	emission	22.16	21.46	0
187	ext#5 F	22:15:55.8	-17:51:56.9	1.2235	0.0001	0	passive	22.19	20.67	0
188	ext#4 K	22:16:03.1	-17:39:18.7	0.9984	0.0004	1	passive	22.19	21.19	0
189		22:16:05.0	-17:50:54.4	1.0647	0.0001	0	emission	22.20	21.38	0
190		22:16:08.2	-17:51:57.0	0.3270	< 0.0001	2	passive	22.21	21.46	0
191		22:15:56.1	-17:50:43.6	0.7796	0.0007	2	passive	22.22	21.00	0
192		22:15:58.0	-17:50:33.2	0	—	0	star	22.23	21.77	0
193	ext#5 D	22:15:56.7	-17:51:32.4	1.2257	0.0001	0	passive	22.23	20.55	0
194	ext#4 M	22:16:11.8	-17:39:57.6	1.0011	0.0003	0	passive	22.23	21.21	0
195		22:15:44.6	-17:48:07.4	0.3899	0.0001	2	passive	22.26	21.74	0
196	ext#4 F	22:15:53.8	-17:40:14.2	0.9946	0.0002	2	emission	22.29	20.93	0
197		22:16:04.3	-17:48:21.1	0.9212	0.0006	1	passive	22.33	21.50	0
198	ext#5 I	22:15:58.0	-17:51:12.6	1.2284	0.0001	1	emission	22.35	22.04	0
199		22:16:03.3	-17:47:47.8	0.9953	0.0003	0	passive	22.37	21.19	0
200		22:15:50.0	-17:52:27.6	0.9582	0.0001	0	passive	22.37	21.30	0
201		22:15:59.2	-17:40:53.5	0	—	0	star	22.40	21.71	1
202		22:15:56.2	-17:40:34.6	0	—	0	star	22.49	20.93	0
203		22:15:51.1	-17:40:34.7	1.0512	0.0002	1	emission	22.50	22.43	0
204	ext#6 K	22:15:09.8	-17:54:35.5	0.4087	< 0.0001	0	emission	22.51	22.63	0
205		22:16:07.3	-17:40:12.0	0.8801	0.0001	0	emission	22.53	21.78	0
206		22:16:10.2	-17:41:15.9	0.7566	0.0003	2	emission	22.55	22.07	0
207		22:15:04.0	-17:54:49.7	0.2277	< 0.0001	0	emission	22.56	22.60	0
208		22:15:53.4	-17:51:12.8	0	—	0	star	22.62	21.87	0
209		22:16:07.7	-17:51:18.7	1.0392	0.0001	0	emission	22.64	21.93	0
210		22:16:10.6	-17:41:19.1	0.5313	< 0.0001	0	emission	22.65	22.11	0
211	ext#5 J	22:15:46.4	-17:52:23.5	1.2252	0.0001	1	emission	22.68	22.41	0
212		22:16:04.3	-17:49:17.9	0.8700	< 0.0001	0	passive	22.70	21.67	0
213		22:16:00.7	-17:49:35.7	1.0487	0.0005	0	emission	22.78	21.99	0
214		22:15:49.8	-17:38:41.0	0	—	0	star	22.82	21.36	0
215	ext#5 L	22:15:47.1	-17:49:08.0	1.2396	0.0001	1	emission	22.89	22.83	0
216		22:16:07.9	-17:47:42.5	0.8644	0.0003	1	emission	22.91	23.17	0
217	ext#5 E	22:15:57.4	-17:51:52.1	1.2232	0.0003	0	passive	22.98	21.33	0
218		22:14:58.6	-17:47:35.8	0	—	0	star	22.98	99.00	0
219		22:15:47.0	-17:39:26.9	1.3285	0.0007	2	passive	23.10	21.29	0
220		22:15:48.8	-17:49:29.1	0.6900	< 0.0001	1	passive	23.18	22.72	0
221		22:15:54.2	-17:51:40.9	0.7082	< 0.0001	0	emission	23.31	23.34	0
222		22:16:04.1	-17:48:34.0	1.3030	0.0003	0	emission	23.35	22.41	0
223		22:15:47.3	+17:39:31.9	0.8290	0.0009	1	passive	23.41	22.79	0
224		22:15:46.2	-17:40:20.9	0.5937	0.0009	1	passive	23.64	23.47	0
225		22:15:57.2	-17:51:23.4	0.4278	0.0006	2	qso	23.88	23.43	0
226		22:15:46.8	-17:51:43.9	1.1545	0.0001	0	emission	23.94	24.05	0
227		22:15:59.8	-17:38:06.7	1.2207	0.0005	0	emission	24.19	23.49	0
228	ext#6 F	22:15:01.0	-17:51:10.8	0.4062	0.0001	2	passive	24.22	23.59	0
229		22:16:00.6	-17:49:39.4	0.9300	< 0.0001	0	emission	24.66	25.50	0
230		22:15:54.1	-17:52:07.3	1.3862	0.0015	2	emission	24.71	24.06	0
231		22:15:51.5	-17:49:11.4	0.3394	< 0.0001	1	emission	26.56	99.00	0